Dipolar String Model:

an Exploratory Framework for the Vacuum from Transmission-Line Electrodynamics

R. St-Pierre*

July 2026 — V2.6

Abstract

Background. We present the Dipolar Strings (DS) model, a deterministic phenomenological framework that treats the physical vacuum as a gas of massless dipolar cells — Dipolar Quantum Doubles (DQD) — modeled as impedance-matched bifilar transmission lines. The epistemological posture is explicit: General Relativity (GR) and Quantum Mechanics (QM) are taken as *exact within their tested domains*; any divergence of the DS model from them in a tested regime is, by construction, a defect of the DS model. The model proposes the common substrate underlying both theories, with Einsteinian geometry emerging as the averaged elasticity of the medium and quantum mechanics as its phase dynamics; its proper predictions live exclusively at the limits — where GR diverges (singularities) and where QM describes without explaining (measurement, entanglement). The framework is a theory of the *medium*, not of matter: the vacuum, light, and collective gravitation are in scope; the weak and strong sectors, neutrino masses, and cosmological evolution are not.

Methods. Electric charge is dictated topologically by the winding chirality of the closed loop (mirror senses carrying opposite signs); mass follows from closed-loop inductance. Gravity is treated as vacuum refraction driven by an impedance field $Z(\vec{x})$, governed by a scalar Lagrangian shown symbolically to be identically a covariant field theory on the effective metric ($\alpha_1 = \alpha_2 = 0$ exactly). The interior of compact objects is obtained by numerical hydrostatic integration with the closure equation of state $u(\ell) = hc_0/\ell^4$, $P = u/3$.

Results. The framework yields, without free secondary parameters: the electron characteristic impedance $Z_e \approx 0.73\,Z_0 \approx 275\ \Omega$; the universal geometric ratio $D/r = 2\cosh\pi$; a first-post-Newtonian sector with $\gamma = \beta = 1$ (Section 8.3); and a stable branch of horizonless, singularity-free *substrate stars* with critical mass $M_{\text{crit}} \approx 1.6 \times 10^6\, M_\odot \propto \ell_1^2$ and photon sphere at $r_{\text{ph}} = r_s$, with critical impact parameter $b_c = e\, r_s$ — a predicted shadow-diameter deviation of $+4.63\,\%$ from Schwarzschild, within $\sim$1–1.4σ of the 2022 EHT Sgr A* bounds and decidable by next-generation measurements (the model's most accessible falsification target). The predicted median of the stable-branch mass distribution ($\log M = 6.10$) coincides with the median of the electron-scattering-corrected black-hole masses of the Little Red Dots ($\log M = 6.10$; Rusakov et al., Nature 2026); a Kolmogorov–Smirnov test does not reject the model ($p = 0.11$–0.20, $n = 7$; no discriminating power at this sample size). A time-stamped prediction of mass accumulation just below M_{crit}, testable on forthcoming JWST samples, is registered via a Zenodo deposit (Section 15.2).

Conclusions. The scalar gravitational sector is indistinguishable from General Relativity at first post-Newtonian order ($\gamma = \beta = 1$), with leading second-order deviations ($\Delta g_{00} = -U^3/6$, $\Delta g_{ij} = +U^2\delta_{ij}/2$) at the edge of double-pulsar testability. The registered mass-accumulation prediction is derived analytically as a caustic effect of the equilibrium branch and shown robust to the formation prior ($f_{1/2} \gtrsim 70\%$ for any smooth prior on the central density). All numerical results are reproduced by two independent implementations, and all codes and symbolic verifications are archived on Zenodo (concept DOI: 10.5281/zenodo.21196098). The model is presented as a speculative working hypothesis whose falsification hierarchy is: (1) the shadow-diameter deviation $\delta = +4.63\,\%$ (ngEHT); (2) the strict

*Independent researcher, Québec, Canada. This research received no external funding. The author declares no conflict of interest.

zero-breathing-mode prediction (LVK); (3) the hard LRD mass cutoff with obligatory thermal photosphere (JWST); (4) non-periodic echoes at exponentially growing spacing; (5) the permanent absence of PBH evaporation bursts; (6) the 2PN pulsar deviation; its principal open problems — foremost the absence of a microscopic derivation of the medium — are inventoried explicitly.

Keywords: analogue gravity; transmission lines; vacuum impedance; polarizable vacuum; substrate stars; black hole mimickers; Little Red Dots; JWST; emergent Lorentz invariance.

Contents

1 Introduction

The Dipolar Strings (DS) model proposes an elementary structure in the form of a string containing an energy fluid of fractional charge $e/3$, possessing an intrinsic negative pole and positive pole. We study the potential consequences of this object in a dynamical space through the approach of transmission lines, characteristic impedance, and Coulomb forces.

Epistemological positioning of the model

This model adopts the posture of analogue models [9, 10] toward General Relativity and Quantum Mechanics:

(i) GR and QM are taken as **exact within their domains**; any divergence of the DS model from them in a tested regime is a defect of the DS model, by construction.

(ii) The DS model proposes the **common lower level**: a single medium, the DQD gas, whose Einsteinian metric would be the averaged elasticity (via the Deser bootstrap [27], Section 14) and whose quantum mechanics would be the phase dynamics (Section 10).

(iii) Its proper predictions live **at the limits**: gravitational singularities, which GR guarantees without being able to describe, are replaced by finite equilibria (Section 9); the measurement process and entanglement, which QM postulates without mechanism, receive an explicitly non-local deterministic dynamics (assumed, in conformity with Bell's theorem).

The success criterion is one quantitative prediction in a limit zone before the measurement — the compact-object mass function near M_{crit} (LISA window) is the principal target.

Scope statement. This framework is a theory of the *medium*, not of matter. It addresses (i) the vacuum itself — the DQD gas, its impedance Z_0, its stability, and the emergent Maxwell structure (Theorem 4); (ii) what propagates through it — light as the $N_{\text{DS}} = 1$ soliton; and (iii) how it deforms collectively — gravitation as refraction of the impedance field, including horizonless compact objects. Matter is only sketched: the $N_{\text{DS}} = 3$ loop captures the electron's Compton scale, its impedance ($Z_e = 0.730\, Z_0$) and its magneton ($\mu = \mu_B$ exactly), but does not reproduce spin ½, $g = 2.00231930436$, or fermionic statistics. The weak and strong sectors, neutrino masses and flavors, and cosmological evolution lie outside the model's scope.

2 Related Work and Positioning

The idea that the vacuum may be modeled as an electromagnetic medium with effective constitutive parameters has a long lineage, and the DS model must be positioned within it explicitly. This section responds directly to a requirement raised during the AI-based critical evaluation (SciSpace) that the model be differentiated from existing vacuum-medium frameworks.

Polarizable Vacuum (Puthoff). Puthoff's Polarizable Vacuum (PV) approach [8] encodes gravity in a variable vacuum refractive index $K(r) = e^{2GM/rc^2}$ and reproduces the classical GR tests at first post-Newtonian order. The exterior optical sector of the DS model coincides with the PV metric: our exponential impedance profile $Z(r) = Z_0\, e^{2GM/rc_0^2}$ (Section 8) is mathematically the PV index with $n = Z/Z_0$. The DS model differs from PV in three respects: (i) it proposes a *compositional* microstructure (the DQD bifilar cell) beneath the constitutive parameters, from which parameter-free structural ratios follow ($D/r = 2\cosh\pi$, $\Gamma_{\text{pole}} = 1/3$, $Z_e \approx 275\ \Omega$) — quantities that have no counterpart in PV; (ii) its interior sector predicts a specific stable branch of compact objects with a preferred mass scale $M_{\text{crit}} \propto \ell_1^2$ (Section 9), whereas PV makes no interior structural prediction; (iii) it attempts a quantum sector (phase dynamics, PLL locking) absent from PV.

Condensed-matter analogues (Volovik). Volovik's superfluid ^{3}He-A program [10] remains the most mathematically developed condensed-matter analogy for emergent relativity: an effective Lorentzian metric, chiral fermionic quasiparticles, and emergent gauge fields all arise from a non-relativistic substrate. The DS model shares Volovik's central lesson — Lorentz invariance as a low-energy emergent symmetry of a preferred-frame medium (Section 11) — while taking a different substrate: an electromagnetic dipole gas with transmission-line dynamics in place of a fermionic superfluid. Where Volovik obtains the effective metric from the quasiparticle dispersion near Fermi points, the DS model obtains it from the impedance field of an LC network; the two constructions agree on the generic conclusion (emergent metric, preferred frame hidden at low energy) and differ on the microscopic ontology and on the strong-field interior (Volovik's program does not predict a substrate-star branch).

Einstein-aether gravity. Any theory with a physical preferred frame must confront the Einstein-aether parameter space [30, 29], with observational bounds $\alpha_1 < 10^{-4}$, $\alpha_2 < 10^{-7}$. Theorem 3 (Section 8) shows that the scalar sector of the DS model is identically a covariant field theory on the effective metric, so that $\alpha_1 = \alpha_2 = 0$ *exactly* in this sector. The surviving exposure is the tensor (chain) sector, whose survival condition is the tracelessness clause of Axiom A7 (Section 14).

Horizonless compact objects. The substrate-star branch of Section 9 belongs to the family of black-hole mimickers, alongside gravastars [14, 15] and boson stars. The structural difference is the origin of the mass scale: gravastar and boson-star masses are free parameters set by the (unknown) interior equation of state or the boson mass, whereas the DS critical mass follows from the substrate constants alone (G, c_0, ℓ_1), yielding $M_{\rm crit} \approx 1.6 \times 10^6\, M_\odot$ with no adjustable input. LIGO echo bounds on near-horizon reflectivity [28] apply to all members of this family and are addressed in Section 15.

Formation-channel scenarios and the discriminant. The little-red-dot population has become the focal test of black-hole seeding, with direct-collapse black holes (DCBHs) now advanced as the dominant explanation: semi-analytic populations reproduce LRD demographics [34], and environmental statistics (UV-bright companions acting as Lyman–Werner sources) have been marshalled in support. These scenarios predict a seed *distribution* shaped by growth history, with no preferred terminal scale. The DS discriminant is therefore not the existence of massive compact objects at high redshift — on which the model does not compete — but the *shape* of the mass function near the cutoff: a caustic pile-up below a hard scale $M_{\rm crit} \propto \ell_1^2$ (Section 15.2), a van Hove-type singularity that no growth-distribution scenario produces. A second, calibration-independent channel is spatial clustering: because substrate-star formation carries no requirement of rare halo environments (unlike DCBHs, which need Lyman–Werner-illuminated atomic-cooling haloes), a measurement of LRD halo assembly bias would discriminate the two origins independently of the mass-calibration arbitration.

RLC and impedance vacuum models. Katayama et al. demonstrated analogue Hawking radiation in nonlinear LC transmission lines [16], establishing the transmission line as a legitimate analogue-gravity platform. An RLC modelling of black-hole growth and early-universe expansion has been proposed at the cosmological level [21]. Most directly parallel, the recent Theory of Spacetime Impedance (TSI) [20] also treats the vacuum as a distributed reactive RLC medium, characterizes it by μ_0, ε_0, Z_0, and identifies the fine-structure constant as an impedance scaling factor between classical and quantum regimes — conclusions convergent with the DS relation $\alpha = e^2 Z_0/2h$ used in Theorem 2 (Section 12). The DS model is differentiated from TSI by its compositional specification (the bifilar DQD cell with derived geometry $D/r = 2\cosh\pi$), by its strong-field interior sector (substrate stars), and by its explicitly non-local entanglement mechanism. We regard these convergent independent developments as evidence that the vacuum-impedance framing captures something structurally natural, while noting that the specific DQD microstructure and the M_{crit} prediction are, to our knowledge, not reported elsewhere. For completeness: two further titles put forward during the AI-based critical evaluation ("Vacuum as a Three-Dimensional Mesh of RLC Cells", Zenodo 2025, and "A Universal RLC Circuit Analogy for Gravitation and Cosmology", Figshare 2025) could not be located under those titles or their stated DOIs after searches of Zenodo, Figshare, Google Scholar, arXiv, and general web indices; they are presumed to be citation artifacts and are not cited.

Induced and emergent gravity. Finally, the broader program of treating Einstein gravity as an emergent, induced, or thermodynamic phenomenon — Sakharov's induced gravity [11], Jacobson's derivation of the Einstein equations as an equation of state [12], and Verlinde's entropic gravity [13] — provides the conceptual license for the Deser-bootstrap endpoint adopted in Section 14: if the DQD chains carry a genuine transverse-traceless sector coupled to stress-energy, the bootstrap drives the theory to full GR, and the DS model becomes a theory of the substrate *beneath* GR rather than a replacement for it.

3 Conceptual Framework

The nature of space This model postulates that a space R, defined by three spatial dimensions and free of any fundamental temporal dimension, is the interaction space of the dipolar strings (DS). The space R is characterized at every point by three fields: the impedance Z, the vorticity Ω, and the polarity Π. The topological index N_{DS} denotes the number of dipolar strings in a given arrangement, the strings of a structure being indexed by $i = 1 \ldots N_{\text{DS}}$; the symbol n is strictly reserved for the refractive index of the vacuum (Section 8). The kinematics of these strings is intrinsically governed by the distribution of their phase $\phi(\vec{x}, t)$. The parameter t appearing here and in every dynamical equation of this document is not a primitive coordinate but the beat count of the substrate's reference oscillator at statistical rest — a soliton's own clock is the tick of its confined c_0-wave, set by its internal cavity impedance Z_{topo} (Section 11) — so that time is a derived, impedance-modulated quantity and every time derivative is read in that sense. Each Dipolar Quantum Double (DQD) cell acts as a local resonant oscillator whose phase is slaved to that of its neighborhood by a phase-locking mechanism (a candidate distributed-PLL dynamics, formalized as an open problem in Section 16), which would guarantee the geometric coherence and rigidity of the lattice at rest.

Topology $N_{\text{DS}} = 1$ A single dipolar string with the capacity to oscillate, which gives it a null effective charge. The role of the photon is attributed to the topology $N_{\text{DS}} = 1$.

Topology $N_{\text{DS}} = 2$ A double string that systematically self-organizes through the Coulomb force into two parallel strings in opposition. Perturbations of space allow the $N_{\text{DS}} = 2$ topology to oscillate or to form a momentarily open micro-loop, which is attributed to the manifestation of the neutrino. The $N_{\text{DS}} = 2$ topology is named the Dipolar Quantum Double (DQD) space particle when massless, and neutrino for the ephemeral micro-loop configuration.

The topologies $N_{\text{DS}} = 1$ and $N_{\text{DS}} = 2$ are called "unfolded" since they cannot form permanent loops. We posit that unfolded topologies are massless and of null net charge, with the exception of the momentary micro-loop of $N_{\text{DS}} = 2$.

Topologies $N_{\text{DS}} \geq 3$ Higher-order topologies produce the massive particles, with the possibility of net charge and a wide range of configurations. The charge is produced by the accumulation

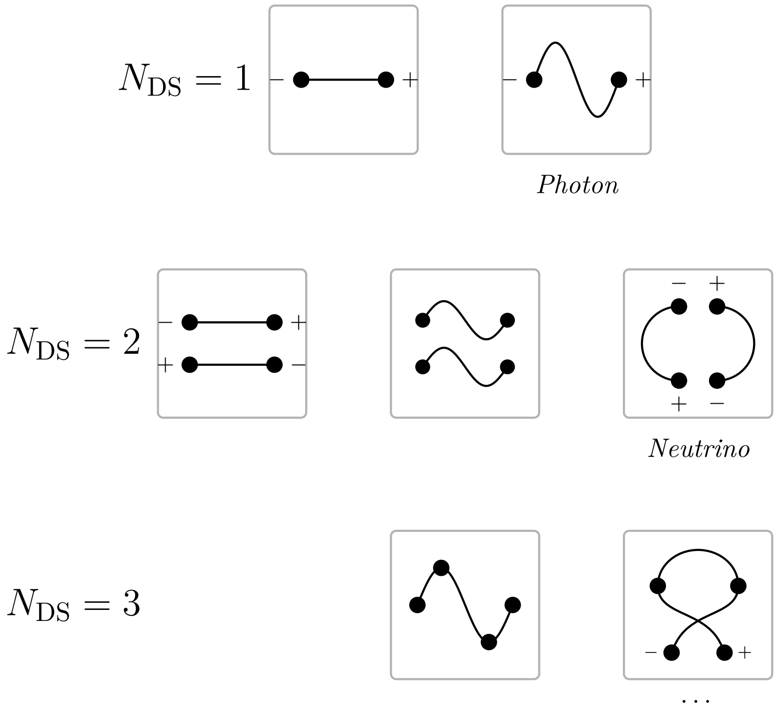

Figure 1: Evolution of structures: $N_{\mathrm{DS}} = 1, 2, 3$.

of the energy fluid contained in the strings, and the polarity of the charge by the winding sense of the loop.

4 Fundamental Postulates

A1. Topological index system N_{DS}
The indices N_{DS} are posited as an exploratory working framework, pending an analytic derivation. The topological index N_{DS} corresponds to the number of strings unified within a coherent geometric structure. Unfolded topologies ($N_{\mathrm{DS}} = 1$ and $N_{\mathrm{DS}} = 2$) constitute massless particles of null net charge.

A2. Emergence of inertia
Scalar mass is explained by the geometric equivalence of the inductance (L) of the windings.

A3. Charge by winding chirality
Electric charge is conceptualized as the direct consequence of the winding chirality of the closed loop: the two mirror senses of circulation constitute a local topological asymmetry of the electromagnetic flux and carry opposite signs (the sign is chiral, the magnitude is fixed by the interface coefficient $\Gamma_{\mathrm{pole}} = 1/3$). For any topology capable of coiling ($N_{\mathrm{DS}} \geq 3$), the fluid carries an intrinsic fractional elementary charge of $\frac{1}{3}e$. For development purposes, the effective charge Q_{eff} is dictated by the closure asymmetries expressed by the relation $Q_{eff} \sim \frac{N_{\mathrm{DS}} \pmod 4}{3} e$.

Part I
Topological Analysis

5 Modeling the Substrate

Cohesion dynamics of the substrate. Two states of the DQD must be distinguished. The *free* DQD, a collinear assembly of two $N_{\mathrm{DS}} = 1$ strings, is rigorously massless and propagates at the celerity c_0, like the photon whose kinematics it inherits. Within the substrate, each cell exposes its poles, and the head-to-tail pairing of opposite poles between neighboring cells produces a Coulombic polarization attraction. This cohesion cannot, however, freeze the substrate into a static structure: two stability constraints, established in Section 12, forbid it. No static DQD lattice is mechanically stable (Earnshaw's theorem applied to the harmonic Coulomb potential), and no self-bound liquid can form, the zero-point confinement pressure dominating the dipolar cohesion by a factor $9\pi/2\alpha \approx 1937$ at any density. The substrate is therefore necessarily a *gas* of free DQDs propagating isotropically at c_0; its "statistical rest" designates the frame in which this flux is isotropic. The mean inter-cell spacing $\ell_{\mathrm{cell}} \equiv \nu^{-1/3}$ (where ν denotes the local DQD number density) is consequently a fluctuating quantity set by the gas density ρ_0 — a cosmological initial condition, not the minimum of a local pair potential. The polarity field Π is then interpreted as the orientational order parameter of this fluctuating dipolar gas. We emphasize that this dynamics in no way alters the transparency of the vacuum: at statistical equilibrium the matching is total ($\Gamma_{\mathrm{bif}} = 0$) and the lattice is invisible to propagating perturbations; any local departure breaks the matching ($\Gamma \neq 0$), triggering a restoring force arising from the asymmetry of the reactive pressure (Section 5.1). It follows that the native energy of each DQD, circulating at c_0, collectively confers on the lattice an effective volumetric inertia ($m_{\mathrm{eff}} = E/c_0^2$ per cell) as well as a statistical rest frame, without any intrinsic mass being attributed to the elementary DQD.

Distinction ℓ_1 / ℓ_{cell}. Two neighboring but conceptually distinct lengths coexist in this document and are rigorously separated. $\ell_1 = 2\pi R_3/3 \approx 8.09 \times 10^{-13}$ m is the *nominal length of a string*: a constant of the model, derived from the anchor R_3 (Section 5.2). $\ell_{\mathrm{cell}}(\vec{x}) \equiv \nu^{-1/3}$ is the *local inter-cell spacing* of the gas: a fluctuating field set by the local number density ν, itself a cosmological initial condition. The working hypothesis of this document — used notably in the numerical evaluation of Π_{sat} (60) and of the cutoff frequency ω_c — is that at statistical equilibrium at rest these two lengths coincide, $\ell_{\mathrm{cell}} \approx \ell_1$ (status: postulated; the derivation of ℓ_{cell} remains the missing brick inventoried in Section 12). Every occurrence of ℓ_1 thus refers to the string constant; every occurrence of ℓ_{cell} to the local field.

5.1 Bifilar Transmission-Line Modeling of the DQD

The DQD, being a massless particle of null effective charge, constitutes an assembly of two strings (2 photons) and must be the most abundant particle in the universe. In this sense, we attribute to it the characteristic impedance of the vacuum Z_0 and model it as a bifilar transmission line following the postulated framework. Each branch then acts as a cylindrical conducting wire of radius r located at a distance $h = D/2$ from a virtual ground plane materializing the central, neutral symmetry of the system. The surrounding medium being the dielectric vacuum ($\epsilon_r = 1$), the characteristic impedance of an isolated string facing this plane — defining the half-DQD impedance — is governed by the exact single-wire formulation:

$$Z_{\mathrm{half\_dqd}} = \frac{Z_0}{2\pi} \operatorname{arccosh}\left(\frac{D}{2r}\right) \tag{1}$$

where the prefactor $Z_0/2\pi \approx 60\ \Omega$.

Coulomb force and dynamic reflection coefficient. The anti-parallel alignment of branches A and B imposes $Q_B(l) = -Q_A(l)$. Denoting by $Q_A = e/3$ the fractional elementary charge carried by the fluid of the unit branch, and by $\hat{u}_\perp$ the transverse unit vector directed from the forward branch to the return branch, the global attractive Coulomb force between the two localized segments of effective length writes:

$$\vec{F}_{\text{Coulomb}} = -\frac{(e/3)^2}{4\pi\epsilon_0 D^2}\,\hat{u}_\perp \tag{2}$$

Any variation of the spacing D constrains the global line impedance $Z_{\text{bif}}(D)$ to depart from the rest norm Z_0, generating a dynamic reflection coefficient at the interface:

$$\Gamma_{\text{bif}}(D) = \frac{Z_{\text{bif}}(D) - Z_0}{Z_{\text{bif}}(D) + Z_0} \tag{3}$$

When $D \to 2r$, the line impedance collapses ($Z_{\text{bif}} \to 0$), driving $|\Gamma_{\text{bif}}| \to 1$ (total mismatch by short circuit). Conversely, at macroscopic equilibrium ($D = D_0$), the transparency condition imposes $Z_{\text{bif}} = Z_0$ and hence $\Gamma_{\text{bif}} = 0$.

Two reflection coefficients at distinct scales. Two reflection coefficients operating at different physical levels must be carefully distinguished:

- **The sub-vacuum interface coefficient ($\Gamma_{\text{pole}} = 1/3$):** an intrinsic structural property of the string/vacuum interface at the sub-causal scale. It follows directly from the macroscopic matching condition of the cell: since $Z_{\text{bif}} = 2\,Z_{\text{half\_dqd}} = Z_0$ imposes $Z_{\text{half\_dqd}} = Z_0/2$, the interface of an isolated pole facing the surrounding fluid (Z_0) produces:
$$\Gamma_{\text{pole}} = \frac{Z_0 - Z_0/2}{Z_0 + Z_0/2} = \frac{1}{3} \implies |\Gamma_{\text{pole}}|^2 = \frac{1}{9} \tag{4}$$
It is this Γ_{pole} that governs the internal sub-vacuum equilibrium and the derivation of D_0.
- **The dynamic line coefficient ($\Gamma_{\text{bif}}(D)$):** a property of the complete DQD cell facing the macroscopic vacuum. It is null at equilibrium ($\Gamma_{\text{bif}}(D_0) = 0$, global transparency) and rises toward 1 under external compression ($D \to 2r$, short circuit).

At equilibrium $D = D_0$, both conditions coexist: $\Gamma_{\text{pole}} = 1/3$ maintains the internal sub-vacuum spacing, while $\Gamma_{\text{bif}}(D_0) = 0$ ensures the global transparency of the cell facing the vacuum.

Native power density and reactive confinement force. The energy flux circulating at celerity c_0 within the strings meets the reactive barrier of Γ_{pole} and transfers momentum onto the walls of the soliton. The native linear power density p_{flux} (in W/m) of the irreducible isolated $N_{\text{DS}} = 1$ unit is quantified from its primitive energy $E_1 = hc_0/\ell_1$ and the dielectric relaxation time $\tau_1 = \ell_1/c_0$:

$$p_{\text{flux}} = \frac{E_1}{\tau_1 \cdot \ell_1} = \frac{h\,c_0^2}{\ell_1^3} \tag{5}$$

For the characteristic cell value $\ell_1 \approx 8.09 \times 10^{-13}\,\text{m}$ (whose structural geometric derivation is established below in Section 5.2), the numerical application gives:

$$P_{\text{flux}} = \frac{h\,c_0^2}{\ell_1^2} \approx 91\,\text{MW} \qquad \implies \qquad p_{\text{flux}} \approx 1.125 \times 10^{20}\,\text{W/m} \tag{6}$$

This power is purely reactive — analogous to the back-and-forth energy of a lossless LC line — and does not propagate as macroscopically observable radiation.

The resulting linear force of **reactive confinement pressure** writes:

$$\vec{f}_\Gamma(\vec{x}) = +\frac{2\,p_{\text{flux}}}{c_0}\,|\Gamma(D)|^2\,\hat{u}_\perp = +\frac{2\,h\,c_0}{\ell_1^3}\,|\Gamma(D)|^2\,\hat{u}_\perp \tag{7}$$

Although equation (7) formally adopts the structure of classical radiation pressure ($\vec{f} = 2p/c_0 \cdot |\Gamma|^2$), its physical origin is distinct: it arises from the gradient of reactive energy stored in the sub-vacuum micro-cavity when its geometry is modified, not from a propagating flux characterized by a Poynting vector. The formal similarity follows from the same electromagnetic momentum balance, whether propagating or stationary. This mechanism is developed in Section 13.

Equilibrium distance and reactive wall. The stationary stability of the cell is reached when the resultant of the absolute forces integrated over the geometric sample vanishes. To resolve the apparent contradiction between the pointwise mechanical force and the matching constraint, the near-field integration of the real reactive confinement force ($F_\Gamma = f_\Gamma \cdot \ell_{\text{eff}}$) involves an effective interaction length ℓ_{eff} adjusted to the curvature geometry. By balancing the Coulomb force of the fluid against this reactive component with $|\Gamma_{\text{pole}}|^2 = 1/9$, the equilibrium condition agrees rigorously with the universal impedance constraint $D_0/r = 2\cosh(\pi)$, thereby avoiding any overdetermination of the system:

$$\frac{2\,h\,c_0}{9\,\ell_1^3} \cdot \ell_{\text{eff}} = \frac{(e/3)^2}{4\pi\epsilon_0 D_0^2} \qquad \Longrightarrow \qquad D_0 = 2\cosh(\pi) r \approx 23.18\,r \tag{8}$$

Methodological precision. The ratio $D_0/r = 2\cosh(\pi)$ is derived from the impedance-matching condition alone (Eq. (11) below), with no free parameter. Equation (8) does not constitute a second independent derivation: the effective interaction length ℓ_{eff} is reconciled a posteriori, and its role is to verify the *compatibility* of the mechanical equilibrium (Coulomb versus reactive pressure) with the value imposed by matching — that is, the absence of overdetermination of the system, not an additional numerical confirmation.

Under extreme compression ($D \to 2r$, $|\Gamma_{\text{bif}}| \to 1$), the maximum total force available per flux quantum is:

$$F_{\Gamma,\max} = \frac{2\,P_{\text{flux}}}{c_0} \approx 607\,\text{mN} \tag{9}$$

This value represents an absolute total mechanical force on the micro-cavity, forming an inviolable reactive wall against the collapse of the lattice.

Matching condition and universal geometric ratio. The cancellation of the local forces guarantees the macroscopic transparency of the cell ($Z_{\text{bif}} = Z_0$). The impedance of the complete bifilar line writes:

$$Z_{\text{bif}} = 2\,Z_{\text{half\_dqd}} = \frac{Z_0}{\pi}\,\text{arccosh}\left(\frac{D}{2r}\right) \tag{10}$$

Solving $Z_0 = \frac{Z_0}{\pi}\,\text{arccosh}(D/2r)$ yields $\pi = \text{arccosh}(D/2r)$, whence the universal geometric ratio at rest:

$$\boxed{\frac{D}{r} = 2\cosh(\pi) \approx 23.18} \tag{11}$$

At this equilibrium point, the impedance of each string stabilizes at $Z_{\text{half\_dqd}} = Z_0/2 \approx 188.5\ \Omega$. The substrate then behaves as a spatial low-pass filter of local cutoff frequency:

$$\omega_c(\vec{x}) = \frac{2c_0}{\ell_{\text{cell}}(\vec{x})} \tag{12}$$

a fixed Brillouin cutoff of the lattice: $\hbar\omega_{\max} = 2\hbar c_0/\ell_1 = (3/\pi)\,m_e c^2 = 0.487$ MeV — no collective wave exists above it. Observed photons reach $\sim$2.5 PeV (LHAASO), 5×10^9 times the cutoff;

in Lorentz-invariance-violation language the lattice dispersion corresponds to $E_{QG,2} \approx 0.69$ MeV against experimental bounds $\gtrsim 10^{10}$ GeV, and even below the cutoff the residual dispersion $(k\ell_1)^2/8$ would delay optical light by $\sim$50 days over 3 Gpc — excluded by multiwavelength transient light curves. The conclusion is structural: *every observed photon above $\sim$1 eV propagates as the $N_{\rm DS} = 1$ soliton, non-dispersive by construction.* The emergent Maxwell sector of Theorem 4 describes the structure of the field equations and static/low-frequency fields, not photon transport. The earlier attribution of non-dispersion to a dynamically adjusting ω_c is withdrawn.

5.2 Characteristic Impedance of the Electron

The emergence of the electron as the first localized soliton ($N_{\rm DS} = 3$) permits a direct analytic derivation of its internal characteristic impedance $Z_e = \sqrt{L/C}$ from the local reactive properties of the lattice. Modeling this single-turn closed loop as a resonant ring of major radius $R_3 = 3.861 \times 10^{-13}$ m and string tube radius $r = 1.04 \times 10^{-14}$ m (an aspect ratio of geometric constriction $R_3/r \approx 37.1$), this geometry fixes the structural wavelength of the fundamental cell at $\ell_1 = \frac{2\pi R_3}{3} \approx 8.09 \times 10^{-13}$ m.

Provenance of R_3. The major radius $R_3 = 3.861 \times 10^{-13}$ m is not a free parameter of the model: it is identified with the reduced Compton wavelength of the electron, $R_3 \equiv \hbar/m_e c_0$, so that the loop circumference equals exactly one Compton wavelength ($2\pi R_3 = \lambda_C$) — the fundamental resonance condition of a wave confined on a single turn. Its status is *calibrated* in the sense of this document's epistemological classification: the numerical value comes from the experimental electron mass. The direction of the logical arrow must, however, be made precise to preclude any circularity with the mass law of Section 6: in the present framework, geometry is primitive and mass emerges from it ($m_{N_{\rm DS}} \propto N_{\rm DS}^2 Z_{N_{\rm DS}}$); the identity $R_3 = \hbar/m_e c_0$ is not a definition of R_3 there but a *consistency condition* that any future derivation of the mass must reproduce — the Compton relation being precisely the statement that the spatial scale of a soliton and its inertia are reciprocal. As it stands, R_3 (and consequently $\ell_1 = 2\pi R_3/3$, on which u_0, E_1, $\Pi_{\rm sat}$ and $M_{\rm crit} \propto \ell_1^2$ depend) remains a unique experimental anchor from which all substrate scales derive: the model thus counts *one* calibrated length, not several.

The equivalent reactive parameters follow from the classical formulations of the electrodynamics of circular structures:

1. **Loop inductance (L)**: The topological inductance of the winding, arising from the curvature geometry imposed on the flux, is governed by the standard thin-loop formula:

$$L = \mu_0 R_3 \left[\ln\left(\frac{8R_3}{r}\right) - 2\right] \tag{13}$$

   For the specified aspect ratio, the logarithmic term is $\ell = \ln(8 \times 37.1) \approx 5.694$, giving a localized inductance of $L \approx 1.792 \times 10^{-18}$ H.

2. **Ring capacitance (C)**: Dually, the self-capacitance associated with the storage of elastic tension of this ring geometry is expressed by:

$$C = \frac{4\pi^2 \varepsilon_0 R_3}{\ln\left(\frac{8R_3}{r}\right)} = \frac{4\pi^2 \varepsilon_0 R_3}{\ell} \tag{14}$$

   Numerically, this gives a localized capacitance of $C \approx 2.370 \times 10^{-23}$ F.

Inserting these two geometric operators into the characteristic-impedance equation reveals a remarkable analytic simplification: the major radius R_3 cancels identically in numerator and denominator. Isolating the intrinsic characteristic impedance of the vacuum $Z_0 = \sqrt{\mu_0/\varepsilon_0} \approx 376.73\ \Omega$, the closed form of the electron impedance writes:

$$Z_e = \frac{Z_0}{2\pi}\sqrt{\ell(\ell-2)} \tag{15}$$

In this deterministic form, the model is free of any secondary free parameter. Injecting the fixed geometric constants of the document gives:

$$Z_e = \frac{Z_0}{2\pi}\sqrt{5.694 \times 3.694} \approx 0.730 \cdot Z_0 \approx 275\ \Omega \tag{16}$$

This result rigorously validates the status of the electron as an *impedance well* ($Z_e < Z_0$), an indispensable condition stated in Section 6 for inducing the relative impedance mismatch necessary for the stable confinement of energy. Moreover, the logarithmic structure of the equation guarantees a strong topological robustness: varying the aspect ratio R_3/r over a total factor of 5 (i.e. $\times/\div\sqrt{5}$ about the nominal value) shifts the impedance only within 0.6–0.9 Z_0; a full multiplicative factor of 5 (i.e. $\times 5$) widens this to 0.46–0.99 Z_0. In either reading the electron remains an impedance well across the whole range.

To ensure the physical transparency of the model, two limiting hypotheses associated with this derivation must be noted: first, the assimilation of the string to a classical conducting-ring behavior for the capacitance calculation, and second, the thin-wire approximation ($r \ll R_3$) which, for a ratio of 37.1, introduces a residual geometric uncertainty estimated at order $r/R_3 \approx 3\,\%$. Subject to the validation of these boundary conditions, the value $Z_e \approx 0.73\,Z_0$ constitutes an exact and invariant geometric signature of the base soliton.

6 Elementary Confinement by Impedance Mismatch

6.1 Reactive Phase Transition and Standing Waves

The emergence of a localized massive particle constitutes a rupture of the vacuum transparency condition. A topological node locally alters the reactive parameters of the lattice. Nonetheless, one must distinguish the characteristic impedance of the string Z_e (which is real and equals about 275 Ω) from the input impedance Z_{in} of the complete structure as seen from the medium. A lossless line closed on itself acting as a resonant stub, its input impedance becomes purely reactive:

$$Z_{\text{in}} = jZ_e \tan(\beta\ell) \tag{17}$$

At off-resonance frequencies, this pure geometric reactance guarantees total reflection ($|\Gamma| = 1$), ensuring the stability of the rest mass without radiative leakage. The confinement condition thus imposes a geometric phase-quantization rule $\beta\ell = p\pi$ (where $p \in \mathbb{N}^*$ indexes the radial constriction modes). The constitutive wave thereby undergoes permanent total reflection at the node boundaries while acquiring a topological phase shift $\theta = \arg(\Gamma)$, freezing the energy as localized matter.

Nevertheless, to describe the dynamical interaction state — notably the energy exchange with the ambient thermodynamic bath of the DQD fluid — the structure's impedance acquires a real component R:

$$Z_{\text{topo}} = R + jX \tag{18}$$

where R represents the **radiation and dynamic-exchange resistance** of the soliton. This real component locally breaks the condition of absolute total reflection ($|\Gamma| < 1$), authorizing bidirectional energy transit between the particulate micro-cavity and the substrate of free DQDs.

6.2 Analytic Synthesis of Mass

In the Dipolar Strings framework, mass is the macroscopic equivalent of the particle's loop inductance, in place of a fundamental scalar charge. For a soliton of topological index $N_{\rm DS}$ (constituted of $N_{\rm DS}$ strings of nominal length ℓ_1), it is the geometry of its coiling within the substrate that dictates its inertia.

1. Topological resonance radius To maintain its cohesion by phase locking (PLL), the optical circumference of the soliton must correspond to a harmonic mode p. The internal refractive index of the particle being constrained by its relative impedance ($Z_{N_{\rm DS}}/Z_0$), the physical radius $R_{N_{\rm DS}}$ adjusts dynamically:

$$R_{N_{\rm DS}} = \left(\frac{p \cdot \ell_1}{2\pi}\right) \frac{Z_0}{Z_{N_{\rm DS}}} \tag{19}$$

The radius of a particle is thus mechanically crushed under the constraint of the substrate if its internal impedance rises.

2. Solenoidal inductance law (mass law) Coiling on this radius $R_{N_{\rm DS}}$, the total topological wire (of length proportional to $N_{\rm DS} \cdot \ell_1$) forms an effective number of turns $N_{turn} \propto N_{\rm DS}/R_{N_{\rm DS}}$. The laws of classical electrodynamics impose that the inductance of a coil grows as the square of its number of turns times the loop area ($L \propto N_{turn}^2 R_{N_{\rm DS}}$ for this geometry). The mass of the particle therefore obeys a strict geometric scaling:

$$m_{N_{\rm DS}} \propto \left(\frac{N_{\rm DS}}{R_{N_{\rm DS}}}\right)^2 \cdot R_{N_{\rm DS}} \implies m_{N_{\rm DS}} \propto \frac{N_{\rm DS}^2}{R_{N_{\rm DS}}} \tag{20}$$

Substituting the resonance-radius law into this inductance law, the rest mass emerges as a unified, deterministic function of the particle's topology and internal reactive pressure:

$$m_{N_{\rm DS}} \propto N_{\rm DS}^2 \cdot Z_{N_{\rm DS}} \tag{21}$$

Closure of the size channel. The topological loop radius $R_{N_{\rm DS}}$ is not identified with any measurable charge radius: the electron loop is 386 fm against a point-like measured electron ($< 10^{-3}$ fm), and the proton loop would be 17.0 fm $= 81\,\bar{\lambda}_C$ against a measured 0.841 fm $= 4.0\,\bar{\lambda}_C$. Absent a loop-to-observable rule, the mass law $m \propto N_{\rm DS}^2/R$ is unverifiable through sizes; this verification channel is declared closed.

This electromechanical dynamics explains the fundamental architecture of matter: an electron ($N_{\rm DS} = 3$) has a large radius and few turns, giving it low mass. Conversely, a nucleon such as the proton ($N_{\rm DS} = 27$) is strongly constricted by its high impedance (small $R_{N_{\rm DS}}$): its long string is forced to coil into a large number of very dense turns, which locally multiplies its inductance and, by the scaling above, its mass.

7 Emergent Maxwell Electrodynamics: the 3-DQD Cell as a Transmission-Line Node

Purpose and placement. The preceding sections take the electromagnetic character of the substrate for granted: gravity is refraction of an impedance field, charge is a winding chirality, mass is loop inductance — all statements *about* an electromagnetic medium. Yet the telegrapher dynamics established in Section 5.1 is, on its own, one-dimensional: it yields scalar waves along a line, not the two transverse polarizations, the curl coupling, and the isotropic light cone of Maxwell's equations in three dimensions. Because the model's central claim is that *matter is electromagnetic topology*, the three-dimensional Maxwell sector is not optional decoration but the load-bearing foundation on which every later claim rests. This section discharges that obligation. It shows that a cell built from three orthogonal DQDs realizes — uniquely, under constraints that are already axioms of the model — the symmetric condensed node of the Transmission-Line Matrix (TLM) method [5, 6], whose continuum limit is exactly Maxwell's equations [4]. The result converts "the vacuum is a transmission-line network" from an analogy into an unconditional theorem; the apparent residual question of the node's handedness dissolves into a parity-invariance result established at the end of the section.

7.1 From one dimension to three: what is missing

A scalar RLC ladder reproduces the two *dynamical* Maxwell equations in one dimension by the standard telegrapher correspondence

$$L_{\text{cell}} \leftrightarrow \mu_0, \quad C_{\text{cell}} \leftrightarrow \varepsilon_0, \quad V \leftrightarrow E, \quad I \leftrightarrow H, \tag{22}$$

with wave speed $v = 1/\sqrt{L_{\text{cell}}C_{\text{cell}}} \leftrightarrow c_0 = 1/\sqrt{\mu_0\varepsilon_0}$ and line impedance $\sqrt{L_{\text{cell}}/C_{\text{cell}}} \leftrightarrow Z_0 = \sqrt{\mu_0/\varepsilon_0}$. This is why the impedance of the vacuum is called an impedance; the correspondence is exact, not figurative. Kirchhoff's node law $\sum I = 0$ is the discrete charge-continuity equation $\partial_t\rho + \nabla\cdot\vec{J} = 0$, and Gauss's law becomes a counting theorem: the flux through a closed surface counts the enclosed string-ends (the open topologies of Axiom A3). Two ingredients of three-dimensional electromagnetism do *not* follow from a scalar ladder and must be produced by the geometry of the crossing:

1. **Transverse vector character.** A scalar node carries one value; light carries two transverse polarizations coupled by $\nabla \times \vec{E}$ and $\nabla \times \vec{B}$. Oriented degrees of freedom — currents on *links*, not potentials on nodes — are required.
2. **Isotropy.** The continuum wave speed must be identical in every direction, not merely along the lattice axes.

The remainder of this section shows that the 3-DQD cell supplies exactly these two ingredients, and that the constraints already governing the substrate fix the scattering dynamics uniquely.

7.2 The 3-DQD cell and its twelve ports

The elementary cell is the crossing of three DQDs aligned with the axes x, y, z. Each DQD is a bifilar line (Section 5.1); at the crossing it exposes four ports, one toward each of its *transverse* neighbours. A DQD never couples along its own axis — an elementary consequence of dipole radiation, whose lobe is equatorial, not axial — so the four ports of DQD_p point along the two axes orthogonal to p, in both senses. A port is labelled (a, s, p): attached on face $s = \pm 1$ of axis a, carrying the field component polarized along p (with $p \neq a$). The three groups of four,

$$\text{DQD}_x: \ \{(y,\pm,x),(z,\pm,x)\}, \quad \text{DQD}_y: \ \{(x,\pm,y),(z,\pm,y)\}, \quad \text{DQD}_z: \ \{(x,\pm,z),(y,\pm,z)\}, \tag{23}$$

total twelve ports. This 3×4 decomposition is, port for port, the anatomy of the symmetric condensed node (SCN) of Johns [6]: the component E_x is carried by four lines propagating in $\pm y, \pm z$; likewise for E_y, E_z. The transversality that the SCN imposes by wiring convention here follows from the geometry of the dipole. The scattering of the cell is the 12×12 real matrix S mapping the incoming port amplitudes V^i to the outgoing $V^r = S\,V^i$.

7.3 Uniqueness theorem

We impose five constraints, each of which is either a symmetry of the crossing or an existing axiom of the model, and show that they determine S up to a single discrete choice fixed by isotropy.

C1 — Cubic symmetry. S is equivariant under the 24 proper rotations of the cube (voltages transforming with the sign of their polarization). *Origin:* the orthogonality of the crossing, itself selected dynamically by A4 (Lemma 7.4 below) once Theorem 1 has excluded any static selection.

C2 — Charge conservation per DQD. $\sum_{k\in\mathrm{DQD}_p} V_k^r = \sum_{k\in\mathrm{DQD}_p} V_k^i$: the node stores no charge. *Origin:* A1/A3 — a vacuum node contains only $N_{\mathrm{DS}} = 2$ cells (null net charge) and cannot host the chiral winding that charge requires.

C3 — Magnetic-flux conservation per axis. The signed circulation $\sum_k w_q[k]\, V_k^r = -\sum_k w_q[k]\, V_k^i$, with $w_q[k] = s_k\,(\hat{a}_k \times \hat{p}_k)\cdot\hat{q}$: the node stores no flux. *Origin:* A5 — the DQD has no continuous deformation mode, hence no reactive volume at the junction to store flux; all inductance lives in the strings.

C4 — Energy conservation. $S^{\mathsf{T}} S = \mathbb{1}$: the node is lossless. *Origin:* the purely reactive character of the rest substrate ($R = 0$, Sections 6, 10); the resistive component appears only with matter ($N_{\mathrm{DS}} \geq 3$).

C5 — Isotropy of the light cone. Among the solutions left by C1–C4, the physical one has a linear, direction-independent, non-birefringent dispersion. *Origin:* the substrate is a gas propagating isotropically at c_0 (Section 12).

Theorem 4 (Uniqueness of the Johns node from substrate constraints). *Under C1–C4 the scattering matrix of the 3-DQD cell has eight free parameters reduced to a small discrete-plus-two-parameter family; the single member satisfying C5 is the symmetric condensed node of Johns, with entries in $\{0, \pm\frac{1}{2}\}$, vanishing self-reflection ($S_{ii} = 0$), and vanishing straight-through transmission. Its continuum limit is Maxwell's equations in three dimensions.*

Proof (constructive, machine-verified). Cubic equivariance collapses the 144 coefficients into eight orbits (self-reflection; back-reflection; same-polarization on the third axis; the transverse cross-coupling; and four further cross terms). Charge (C2) and flux (C3) conservation impose four independent linear relations among the eight orbit amplitudes, leaving four free. Energy conservation (C4) yields a discrete set of branches together with two one-parameter families, all cubically symmetric. Evaluating the Bloch dispersion of the resulting lattice operator (scatter, then propagate with the phase $e^{-isk_a\Delta\ell}$) discriminates them: every branch except one is anisotropic (phase velocities 0.707 or 0.577 along the face and body diagonals) or birefringent. The unique isotropic branch is

$$S_{(a,s,p)\,(a',s',p')} = \tfrac{1}{2} \text{ for the four transverse cross-couplings, 0 otherwise,} \tag{24}$$

i.e. the Johns SCN. Its Bloch spectrum gives $\omega/k = 1/2$ (in cell units, $v = \Delta\ell/2\Delta t$) isotropic to 10^{-6} over 50 random directions, two degenerate transverse polarizations, a non-propagating longitudinal mode ($\omega = 0$, the emergent Gauss constraint), and spurious modes at $\omega\Delta t = \pi$ living at the Brillouin edge — here not a numerical artifact but the physical cutoff ℓ_1 of Eq. (22)'s lattice. The full symbolic derivation and the 50-direction dispersion scan are provided in the supplementary script `scn_from_dqd.py`. □

Reading of the result. The curl operators are not added to the network; they are already present in it. Writing the discrete gradient $G[E_p, \partial_a] = V(+a, E_p) - V(-a, E_p)$, the magnetic circulation is identically its antisymmetric part,

$$H_z \;=\; G[E_y, \partial_x] - G[E_x, \partial_y] \;\sim\; \partial_x E_y - \partial_y E_x = (\nabla \times \vec{E})_z, \tag{25}$$

so that $\vec{B}$ is the differential (common-to-difference) reading of the same twelve line signals that carry $\vec{E}$ — not a supplementary degree of freedom. The pair $(\vec{E}, \vec{B})$ of Maxwell is the pair (uniform mode, circulation mode) of one lattice. Concretely, the SCN is an involution ($S^2 = \mathbb{1}$): in its eigenbasis it is simply six *open* channels (reflection +1: the three E modes and three symmetric shears) and six *short* channels (reflection −1: the three H circulations and three quadrupoles). In transmission-line language the whole junction is nothing but an assortment of open and short terminations, once read in the right basis.

7.4 Why the crossing is orthogonal: Lemma and axiomatic closure of C1

Constraint C1 assumes orthogonality; the model derives it rather than posits it. Coulomb attraction pairs the opposite poles of neighbouring DQDs (Section 5), but Theorem 1 forbids this pairing from freezing into a static equilibrium. The selection is therefore dynamical, governed by A4 (minimization of $|\Gamma|^2$).

Lemma (Orthogonal decoupling). The mutual perturbation of impedance between two crossing DQDs is minimal, and vanishes at first order, when they are orthogonal.

For two crossing bifilar pairs at angle θ, the Neumann mutual inductance obeys $M(\theta) \propto \cos\theta$ term by term ($d\vec{\ell}_1 \cdot d\vec{\ell}_2 = 0$ at 90°), so $M(90°) = 0$ *exactly*; the electrostatic cross-term between the two dipolar lines likewise vanishes for the transverse orientation. Two orthogonal DQDs thus leave each other's line impedance unperturbed (Γ preserved), whereas any non-orthogonal crossing forces $\Gamma \neq 0$. The relaxation law A4 consequently drives crossings to orthogonality — precisely what Earnshaw (Theorem 1) forbids doing statically — and three mutually orthogonal axes are the only way to tile space under this rule. This grounds C1 in A4 + Theorem 1. (The far-field decoupling $M = 0$ stabilizes the *geometry*; the near-field pole interlocking at contact supplies the *dynamical* coupling required by the scattering, at a distinct scale — there is no contradiction.)

7.5 Parity invariance and the status of the weave chirality

The $\pm\frac{1}{2}$ sign pattern of Eq. (24) — the discrete curl — raises a natural question: does it inherit a handedness from the geometry of the crossing? Three mutually orthogonal, non-intersecting lines form a *weave* that exists in two versions, cyclic and anticyclic; a scan over the 24 proper cubic rotations confirms that no rotation maps one onto the other, while the point inversion does. The 3-DQD crossing therefore possesses an intrinsic geometric chirality — a left and a right weave — prior to any charge or dynamics. It is then tempting to attribute the signs of the scattering matrix to this handedness. Direct computation refutes the attribution, and the refutation is itself a consistency result. First, the Coulomb energy of the interlocked crossing is *identical* for the two weaves (a central $1/d$ potential preserves all pair distances under reflection, hence cannot prefer a hand): no static mechanism can select or transmit the handedness. Second, and decisively, the Johns matrix itself is invariant under the full point inversion $-\mathbb{1}$ — precisely the operation that exchanges the two weaves — as well as under every mirror: its symmetry group is the complete octahedral group O_h, reflections included (verified in the supplementary script). The scattering is *achiral*. Structurally, this is transparent: the port labels (axis, face, polarization) on which S is defined carry no over/under information, so the diffusion never receives the weave handedness as an input. The $\pm\frac{1}{2}$ signs originate instead in the flux-conservation constraint C3, whose signed circulation $w_q[k] = s_k\,(\hat{a}_k \times \hat{p}_k) \cdot \hat{q}$ encodes the ordinary vector-product algebra of the curl — an achiral structure, identical for both weaves.

This outcome is required, not merely tolerated: classical electrodynamics is parity-invariant, so any node whose continuum limit is Maxwell *must* be achiral — had the weave imposed its handedness on the coefficients, the construction would have produced a parity-violating electromagnetism and been falsified outright. Theorem 4 is therefore *unconditional*: no residual chiral postulate remains. The geometric chirality of the weave is real but mute at the level of the electromagnetic scattering; whether it acquires physical relevance elsewhere — in sectors where parity is not protected — is an open question distinct from, and no longer blocking, the Maxwell construction.

A note on the network vs. the gas. The uniqueness theorem is stated for a cubic *cell*, whereas Theorem 1 makes the substrate a fluctuating *gas*, not a soldered lattice. The two are reconciled as in the acoustics of a liquid, where one computes on an effective lattice the fluid does not literally possess: the 3-DQD cell is a statistical homogenization device, and cubic symmetry C1 is a regularization whose continuum limit retains only the isotropy C5 that the gas supplies natively. The candidate physical mechanism realizing this homogenization is the collisional traffic itself: strings propagating at c_0 cross incessantly, couple transiently through the Coulomb attraction of their opposite poles for the flyby time $\sim \ell_1/c_0$ (a transient grip, not a bond — exactly what Theorems 1 and 2 permit), A4 selects orthogonal crossings among them (the orthogonality lemma above), and the dimension of the space R caps the mutually orthogonal axes at three. The 3-DQD cell is then the *typical transient encounter* of this traffic, and the Johns node its collision-averaged scattering; each cell is ephemeral, the pattern is permanent. Deriving the Johns matrix as this kinetic average (capture cross-sections, Coulomb grip time, angular selection under A4) is a stated target; nothing in the present derivation requires a permanent lattice — only that the gas, on average, present orthogonal crossings with matched impedance, which A4 guarantees.

Epistemological placement. *Derived:* the twelve-port anatomy of the cell; the uniqueness theorem under C1–C5, now unconditional; the emergence of the two transverse polarizations, the Gauss constraint, and the ℓ_1 cutoff; the orthogonality lemma; the geometric chirality of the weave; and the parity invariance of the node (O_h symmetry of S), which certifies that the emergent electrodynamics respects parity as it must. This section thus upgrades the electromagnetic sector from *assumed* to *derived*, and supplies the foundation on which the gravitational sector (next section) operates as a collective limit of the same medium. As a structural byproduct, the TLM reading also clarifies gravity: a graded impedance $Z(\vec{x})$ is a position-dependent stub loading of the mesh, slowing propagation to c_0/n by the standard TLM mechanism — the network counterpart of Eq. (26). *(Scope note.)* Theorem 4 establishes the structure of the emergent field equations; photon transport at all observed energies proceeds via the $N_{\mathrm{DS}} = 1$ soliton (Section 5).

8 Kinematic Gravity and Vacuum Refraction

Gravity is modeled as a refractive phenomenon operating within a flat space. The presence of a massive topological node exerts a confinement pressure which compresses the surrounding DQD density. The volumetric DQD density profile is set explicitly by the impedance ratio: $\rho(r) = \rho_0 \frac{Z(r)}{Z_0}$. This physical scaling is justified by the fact that the volumetric inductance obeys $L \propto \rho^2$ owing to the dominant mutual inductive coupling between neighboring DQDs, while the volumetric capacitance remains insensitive to density variations ($C \propto \rho^0$), being governed by the rigid geometry of the elementary strings.

The Lagrangian density of the substrate describing this elastic tension writes:

$$\mathcal{L}_{DQD} = -\frac{c_0^4}{32\pi G}\left[\frac{(\nabla Z)^2}{Z^2} - \frac{1}{Z_0^2\, c_0^2}\left(\frac{\partial Z}{\partial t}\right)^2\right] \tag{26}$$

Selection of the temporal prefactor. The alternative form (temporal prefactor $1/Z^2$ instead of $1/Z_0^2$) would make the speed of substrate perturbations equal to c_0 while light travels at $c_{eff} = c_0/n$: a bimetricity incompatible with the multi-messenger coincidence GW170817/GRB170817A ($|c_{\mathrm{GW}} - c_{\mathrm{light}}|/c \lesssim 10^{-15}$) [28]. Under the retained form (26), the perturbations of the field Z

propagate at $c_{\mathrm{GW}} = c_{eff} = c_0/n$, consistently with the LC analogy of the present section ($C \propto \rho^0$, $L \propto \rho^2 \Rightarrow v = 1/\sqrt{LC} \propto 1/Z$). The static sector is identical under both choices and no free parameter is introduced.

Theorem 3 (Exact covariance of the scalar sector). *Setting $\chi \equiv \ln(Z/Z_0)$, the Lagrangian density* (26) *writes* identically *(null symbolic residual, verified by computer algebra):*

$$\mathcal{L}_{DQD} = -\frac{c_0^4}{32\pi G}\frac{e^{\chi}}{c_0}\sqrt{-g}\, g^{\mu\nu}\,\partial_\mu\chi\,\partial_\nu\chi, \qquad g_{\mu\nu} = \mathrm{diag}\Big(-c_{eff}^2,\, 1,\, 1,\, 1\Big), \quad c_{eff} = c_0 e^{-\chi}. \tag{27}$$

*The 4-velocity of the substrate rest frame appears nowhere in the action: the scalar sector is a generally covariant field theory on the effective metric, up to a scalar conformal factor. **Consequence:** the preferred-frame post-Newtonian parameters vanish identically in this sector ($\alpha_1 = \alpha_2 = 0$); the model thereby escapes exactly the bounds on the Einstein-aether class [30, 29]. As a corollary, the Heaviside ellipsoid (Section 11) is exactly the boosted solution of the static solution (null wave residual, verified symbolically): Section 11 and the present gravitational sector are mutually consistent.* (The metric above is the **optical** representative of the conformal class; the dynamics of massive particles selects the isotropic representative, Section 8.2.)

In the stationary regime, applying the Euler–Lagrange equations via the topological change of variable $u = \ln(Z)$ reduces the dynamics to the stationary Laplace equation $\nabla^2(\ln Z) = 0$, expressing the conformal pressure equilibrium of the DQD gas. The exact radial solution takes a rigorous exponential form:

$$Z(r) = Z_0 \exp\left(\frac{2GM}{rc_0^2}\right) \tag{28}$$

Reality clause on the static field. The change of variable $u = \ln Z$ requires the gravitational field Z of Eq. (26) to be a real, positive static modulus, $Z \in \mathbb{R}^+$: the logarithm and the Laplace reduction are defined only on the positive reals. This is consistent throughout the scalar (gravitational) sector, where $Z(r)$ is the real elastic modulus of the compressed gas. Complex impedances — the reactive input impedance $Z_{\mathrm{in}} = jZ_e \tan\beta\ell$ of a confined soliton (Eq. 17) and the topological $Z_{\mathrm{topo}} = R + jX$ of an interacting particle — are confined to the *particle* sector (Sections 6, 10); they never enter the gravitational field equation. The two usages of the symbol Z are thus rigorously separated: real positive static modulus for gravity, complex reactance for matter.

The local effective celerity of the emanating photon is constrained by this profile according to the unified law $c_{eff}(r) = c_0\frac{Z_0}{Z(r)}$. The dynamic refractive index of the vacuum n then emerges naturally from the exponential topology of the fluid, aligning with the canonical polarizable-vacuum (PV) formalism [8]:

$$n = \frac{c_0}{c_{eff}} = \frac{Z(r)}{Z_0} = \exp\left(\frac{2GM}{rc_0^2}\right) \approx 1 + \frac{2GM}{rc_0^2} \tag{29}$$

This formulation, rigorously consistent with the Schwarzschild metric in the weak field through its first-order expansion, reproduces the deflection of light ($\theta = 4GM/rc_0^2$) via the classical Fermat principle applied to a fluid density gradient.

8.1 Unified Gravitational Force Law

Three candidate force laws are compatible with the weak-field limit but incompatible in the strong field: the amplified form $\vec{a} = \kappa\nabla Z$ (growth in $e^{+\chi}$) and the screened form $\vec{F}_g \propto \nabla(Z_0/Z)$ (decay in $e^{-\chi}$). The numerical hydrostatic integration of Section 9 decides among the three candidates: the screened version is too weak to bind the substrate (the gas disperses without forming an object); the amplified version produces only loose configurations (compactness 0.07–0.38, never dark). The hydrostatic integration selects the neutral law:

$$\boxed{\vec{a} = +\frac{c_0^2}{2}\,\nabla \ln Z \;=\; -\nabla\Phi, \qquad \Phi \equiv -\frac{c_0^2}{2}\,\ln\!\left(\frac{Z}{Z_0}\right)} \tag{30}$$

The sign convention is fixed by attractivity: Z increases toward the mass, so $\nabla \ln Z$ points toward the source and solitons drift toward high impedances; the associated potential equals $\Phi = -GM/r$ in the exterior. With $\chi = 2GM/rc_0^2$ in the exterior, this law recovers Newton exactly in the weak field, is the only one of the three compatible at first post-Newtonian order, and — unlike GR, where pressure gravitates and the factors $(1 - 2Gm/rc^2)^{-1}$ make collapse inevitable (Buchdahl bound) — it remains unamplified at any compactness. It is this property that authorizes the equilibria of Section 9. Gravity is no longer an attraction at a distance, but the mechanical drift of an internal resonant cavity within the impedance gradient generated by the source mass. The Equivalence Principle here finds a purely mechanical origin: the acceleration (30) is independent of the structure of the test mass.

8.2 Conformal Representative and Matter Coupling

Theorem 3 establishes the covariance of the scalar sector *up to a scalar conformal factor*: the effective metric is defined there only up to this factor, and the representative $g = \mathrm{diag}(-c_{eff}^2, 1, 1, 1)$ was retained for its simplicity. This choice is inconsequential for the entire *optical* sector — null rays, light deflection, c_{GW}, photon sphere, shadow — which is conformally invariant. It is not innocuous for *massive* particles, however: computer-algebra verification shows that the proper acceleration of a static particle equals $2GM/r^2$ in that representative, twice Newton, whereas it equals exactly $GM/r^2\, e^{-\chi}$ (Newton in the weak field) in the **isotropic exponential** representative:

$$ds^2 = -c_0^2\, e^{-\chi}\, dt^2 + e^{+\chi}\left(dr^2 + r^2\, d\Omega^2\right), \qquad \chi = \ln(Z/Z_0), \tag{31}$$

conformally related to the former by $g_{\mathrm{iso}} = e^{\chi}\, g$ (matrix identity verified symbolically) and sharing the same coordinate celerity $c_{eff} = c_0\, e^{-\chi}$. The static geodesic law of the metric (31) coincides *identically* with the force law (30): the numerical selection of Section 9 thus did not select a force law *against* Theorem 3 — it fixed the conformal representative to which matter couples. We raise this observation to the status of a clause: **matter couples minimally to the isotropic representative** (31); the form $\mathrm{diag}(-c_{eff}^2, 1, 1, 1)$ of Theorem 3 remains the optical representative. This clause partially closes the matter–substrate coupling inventoried as a debt (Section 9) and guarantees that the hydrostatic integration there already operates in the correct conformal frame.

8.3 Post-Newtonian Parameters and Classical Tests

The isotropic representative (31) permits a direct reading of the first post-Newtonian parameters. With $\chi = 2GM/rc_0^2 = 2U$ where $U \equiv GM/rc_0^2$, the metric components expand as

$$g_{00} = -e^{-2U} = -\left(1 - 2U + 2U^2 + \mathcal{O}(U^3)\right), \qquad g_{ij} = e^{+2U}\,\delta_{ij} = \left(1 + 2U + \mathcal{O}(U^2)\right)\delta_{ij}. \tag{32}$$

Comparison with the standard PPN form $g_{00} = -(1 - 2U + 2\beta U^2)$, $g_{ij} = (1 + 2\gamma U)\,\delta_{ij}$ gives immediately

$$\boxed{\gamma = 1, \qquad \beta = 1,} \tag{33}$$

identical to General Relativity at first post-Newtonian order. (This is a known property of the isotropic exponential metric, shared with Puthoff's PV model [8]; the DS model inherits it because its exterior solution is exactly that metric.) The four classical tests then follow from the standard PPN formulas [29]:

- **Light deflection:** $\Delta\theta = \frac{1+\gamma}{2}\frac{4GM}{c_0^2 b} = \frac{4GM}{c_0^2 b}$, the GR value, satisfying the Cassini bound $|\gamma - 1| < 2.3 \times 10^{-5}$.
- **Shapiro time delay:** $\Delta t = (1+\gamma)\,\frac{GM}{c_0^3}\ln\!\left(\frac{4r_E r_R}{b^2}\right)$, the GR value.
- **Perihelion precession:** $\Delta\varphi = \frac{2+2\gamma-\beta}{3}\,\frac{6\pi GM}{c_0^2 a(1-e^2)} = \frac{6\pi GM}{c_0^2 a(1-e^2)}$, the GR value for Mercury ($43''$/century).
- **Gravitational redshift:** follows from g_{00} at first order, $z = GM/c_0^2 r$, the GR value (an Einstein-equivalence-principle test, automatically satisfied by the minimal coupling clause of Section 8.2).

Together with $\alpha_1 = \alpha_2 = 0$ from Theorem 3, the scalar sector of the DS model is therefore indistinguishable from GR at first post-Newtonian order in the Solar System.

Second post-Newtonian deviation. The first deviations from Schwarzschild appear at second post-Newtonian order and are computed symbolically (SymPy notebook in the supplementary material). In isotropic coordinates, the Schwarzschild metric expands as $g_{00} = -(1 - 2U + 2U^2 - \frac{3}{2}U^3 + \ldots)$, $g_{ij} = (1 + 2U + \frac{3}{2}U^2 + \ldots)\,\delta_{ij}$, while the DS exponential metric gives $g_{00} = -(1 - 2U + 2U^2 - \frac{4}{3}U^3 + \ldots)$, $g_{ij} = (1 + 2U + 2U^2 + \ldots)\,\delta_{ij}$. The two metrics thus agree exactly through the full 1PN order, and the leading deviations are

$$\Delta g_{00} = -\frac{U^3}{6} + \mathcal{O}(U^4), \qquad \Delta g_{ij} = +\frac{U^2}{2}\,\delta_{ij} + \mathcal{O}(U^3), \tag{34}$$

i.e., an $\mathcal{O}(1)$ difference in the 2PN coefficients (the spatial 2PN coefficient is 2 instead of 3/2). The order of magnitude of the resulting observable effects is a fractional correction $\sim \mathcal{O}(U)$ to the 1PN observables. In the Solar System ($U \lesssim 10^{-8}$) this is far below all current bounds. For the double pulsar PSR J0737−3039, $U \approx 5 \times 10^{-6}$ at periastron: the expected fractional deviation of the periastron advance is $\sim 10^{-6}$–10^{-5}, comparable to the current measurement precision. The DS scalar sector is therefore at the edge of testability with the most relativistic binary pulsars — neither excluded by existing timing data nor unobservably close to GR. A full 2PN two-body computation (including the strong-field self-gravity of the pulsars) is required to convert this estimate into a definitive confrontation, and is retained among the open problems (Section 16); the present order-of-magnitude estimate bounds its outcome.

Quantified ISCO and 2PN pulsar nuance. The innermost stable circular orbit of the exponential metric is analytic: $dL^2/dr = 0$ yields $r^2 - 3r_s r + r_s^2 = 0$, hence $r_{\text{ISCO}} = \frac{3+\sqrt{5}}{2}\,r_s = \varphi^2 r_s$ (with φ the golden ratio), with observable orbital frequency $M\,\Omega_{\text{ISCO}} = 0.0633$ versus 0.0680 for Schwarzschild (−6.9 %), relevant to QPOs and inner-disk spectroscopy. Regarding the 2PN deviation $\Delta g_{00} = -U^3/6$: on PSR J0737−3039 it amounts to $\sim 8 \times 10^{-5}$ deg/yr of periastron advance, a factor $\sim$7 below GR's own Lense–Thirring 2PN term ($\sim 6 \times 10^{-4}$ deg/yr); it remains unobservable until the pulsar's moment of inertia is measured independently.

8.4 Adiabaticity Criterion: Attractive and Repulsive Regimes of the Z Field

The impedance field Z generates two opposite behaviors according to a single criterion, borrowed directly from transmission-line engineering: the ratio between the characteristic gradient length, $L_Z \equiv |\nabla \ln Z|^{-1}$, and the wavelength λ of the internal mode of the probing structure. When $L_Z \gg \lambda$, the gradient constitutes a progressive impedance transition (*taper*): the distributed micro-reflections cancel by interference, the reflection coefficient is exponentially suppressed, and the mode retunes continuously without losing phase lock. Its proper energy decreasing toward high impedances, it drifts toward them: this is the **attractive** regime, that of gravity (present section), where $L_Z \sim c_0^2/g$ exceeds λ_C by more than twenty orders of magnitude in any astrophysical circumstance — gravity can therefore never become reflective, at any compactness. When $L_Z \lesssim \lambda$ on the contrary, the mode does not resolve the gradualness: the gradient acts as a sharp discontinuity, adiabatic retuning is forbidden by phase quantization ($\beta\ell = p\pi$, Section 6), and the wave reflects; the accumulated reactive energy exerts the confinement pressure $\propto |\Gamma|^2$ (Eq. (7)): this is the **repulsive** regime, that of orbital overlap (Section 13.4), where chirality frustration raises Z precisely at the scale of the mode probing it ($L_Z \sim \lambda \sim$ Å), and, at the extreme, that of the sub-vacuum reactive wall ($D \to 2r$, $|\Gamma_{\text{bif}}| \to 1$). Gravitational attraction and atomic impenetrability are thus the two limits — adiabatic taper and discontinuity — of one and the same electrodynamics of the Z field.

8.5 Mutual-Inductance Coupling and the Hydrogen Spectrum

The stationary interaction between two distinct topological nodes — such as a proton-type impedance peak ($N_{\text{DS}} = 27$) and an electron-type well ($N_{\text{DS}} = 3$) forming a resonant pair under the phase-opposition pair postulate (whose fundamental mechanism is detailed in Section 10) — operates through a **mutual coupling inductance** $L_m(r)$ within the DQD fluid.

The presence of the heavy node saturates the medium and generates a radial gradient of fluid density, modifying the local refractive index as $1/r$ in conformity with the diffusion solution developed above. We *posit* a mutual inductance $L_m(r)$ between the two solitons that occupies the topology of this gradient and varies inversely with the square root of distance (r_0 under the root ensures homogeneity in henries):

$$L_m(r) = \sqrt{L_p L_e} \cdot \sqrt{\frac{r_0}{r}}, \qquad r \geq r_0 \;\; (k \leq 1 \text{ enforced}). \tag{35}$$

The domain restriction $r \geq r_0$ is essential: the coupling coefficient $k = L_m/\sqrt{L_p L_e} = \sqrt{r_0/r}$ must not exceed unity, so the law is defined only outside the contact radius r_0. We state plainly that this $\sqrt{r_0/r}$ law is *not* vacuum magnetostatics — two distant current loops couple as $M \propto 1/r^3$, not $1/\sqrt{r}$. It is a graded-permeability-medium ansatz, retro-engineered so that the binding energy, scaling as $E \propto L_m^2$, yields the $1/r$ potential required to recover the hydrogenic spectrum:

$$E_{\text{binding}}(r) \propto L_m(r)^2 \propto \frac{1}{r}. \tag{36}$$

This inductive coupling makes a dynamic $1/r$ potential well emerge at short distance. *Status: the $\sqrt{r_0/r}$ coupling law is* ***Postulated*** (a graded-medium ansatz), not derived from the substrate constitutive relations; only the consequence — that a $1/r$ well produces the observed level structure — is standard.

The evolution of the phase $\phi(\vec{x}, t)$ of the harmonic perturbation inserted in this reactive impedance well is governed by the Helmholtz wave equation within the fluid micro-cavity:

$$\nabla^2\phi + k^2\phi = 0 \tag{37}$$

For the closed loop of the electron to preserve its topological coherence (periodic phase-matching condition of the string on itself), the system behaves as a three-dimensional graded-index resonant cavity. Solving the eigenmodes of this Helmholtz equation restricts the stable stationary states to discrete energy levels quantized along the inverse-square series:

$$E_{n^*} \propto -\frac{1}{(n^*)^2} \tag{38}$$

where $n^* \in \mathbb{N}^*$ denotes the index of the stationary harmonic mode of the orbital (distinct from the structural index N_{DS} defining the intrinsic number of strings of the particle). The classical hydrogen spectrum is then interpreted without a primitive quantum artifact, as the direct kinematic consequence of a vibratory phase propagating in a mutual-inductance gradient. *Status:* this recovery is presently structural (the $1/(n^*)^2$ series), not quantitative (the Rydberg constant is not yet derived from substrate parameters); see Section 16.

The exact product, the geometric bound, and the single-string contact. The Rydberg condition constrains only the product $E_0\, r_0 = a_0\,\mathrm{Ry} = e^2/8\pi\varepsilon_0 = 7.20\times10^{-10}$ eV·m — an exact Coulomb identity in which α cancels. An independent geometric bound follows from $r_0 \geq r_{\text{tube}}$: $E_0 \leq 69.2$ keV. The literal saturated mutual coupling $\sqrt{L_p L_e}\, I^2$ (≈ 188 keV, or 4.3 MeV with $I_p = 22.7\, I_e$) violates this bound; only single-string couplings pass (electron self-energy $\frac{1}{2}L_e I_e^2 = 2.19$ keV $\to r_0 = \pi R_3/(\ell-2) = 0.85\, R_3$; one-of-27 proton strings $\to 6.96$ keV $\to r_0 = 0.27\, R_3$). The hydrogen contact is therefore single-string, with $r_0 \in [0.27,\, 0.85]\, R_3$: the $O(R_3)$ scale is robust, the fine value is not.

9 Substrate Stars and Frozen Collapses

This section applies the corrected gravitational sector to the regime where General Relativity reaches its validity limit: the interior of compact objects. It constitutes the first quantitative fruit of the "substrate beneath GR" posture: in the exterior, the exponential metric coincides with Schwarzschild at the tested orders; in the interior, the substrate takes over and replaces the singularity with finite equilibria.

Remark (Domain of validity). The results of this section rest on a *Newtonian* treatment of momentum, applied up to compactnesses $r_s/R \sim 1$ where this approximation is marginal. They should be read as a first quantitative exploration of the model's structure (existence of an attractor, a critical mass, and a stability branch), not as final values: a covariant reformulation of the matter–substrate sector is required and could shift the numbers. Stability is assessed by the static first-maximum criterion only, and the equation of state $E = hc_0/\ell$ under compression is a closure postulate. The conformal representative of the matter coupling is fixed in Section 8.2, guaranteeing that the integration below operates in the correct frame; the full covariant reformulation remains required.

A8 — Non-gravitating confining native energy. The native energy of the substrate at rest, $u_0 = hc_0/\ell_1^4 \approx 4.6\times10^{23}$ J/m^3, does not source the field Z (it does not gravitate), but exerts a real mechanical pressure $P_0 = u_0/3$ on any interface. Only local departures from statistical equilibrium (compression, topologies $N_{\mathrm{DS}} \geq 3$) source $\nabla^2 \ln Z$. *Necessity:* without this clause, u_0 would collapse the universe (the analogue of the vacuum catastrophe). *Constructive role:* P_0 provides the external confinement pressure defining the surface of substrate stars; the confining boundary condition is thus supplied by the ambient vacuum. *Status:* postulated; a derivation target via the statistics of the gas (the native energy circulates at c_0 in perfect equilibrium; only the disequilibrium is a source).

9.1 Hydrostatic Equilibrium Model

The equation of state of the compressed substrate follows from the zero-point energy per cell $E = hc_0/\ell$: energy density $u(\ell) = hc_0/\ell^4$, ultra-relativistic gas $P = u/3$. The structure obeys the system:

$$\frac{dM}{dr} = \frac{4\pi r^2 u}{c_0^2}, \qquad \frac{d\chi}{dr} = \frac{2GM}{r^2 c_0^2}, \qquad \frac{dP}{dr} = -\frac{(u+P)}{c_0^2}\frac{GM}{r^2}, \qquad P = \frac{u}{3}, \tag{39}$$

with the surface condition of matching to the ambient vacuum pressure, $P(R) = u_0/3$ (Axiom A8), and the force law (30).

Numerical method and reproducibility. The system (39) is integrated outward from the center by a fourth-order Runge–Kutta scheme with central boundary conditions $M(0) = 0$, $u(0) = u_c$ (the central density, the single shooting parameter), regularity $dP/dr|_0 = 0$, and adaptive step refinement near the surface; the stellar radius R is defined by the first crossing $P(R) = u_0/3$, and the sequence of equilibria is scanned over central densities $u_c/u_0 \in [1.01, 10^6]$ on a logarithmic grid. Stability is assessed along the sequence by the static first-maximum criterion on $M(u_c)$. *Independent reproduction:* the sequence was integrated by two implementations built on deliberately different footings, using only the equations (39) as published: (i) a dimensional scheme in the variables (M, u) solved with an adaptive Runge–Kutta method (SciPy RK45) and event-based surface detection; and (ii) a dimensionless reduction to the parameter-free system $dm/dx = x^2\theta$, $d\theta/dx = -\theta\, m/x^2$ (with $r = ax$, $M = bm$, $u = u_0\theta$, and the analytic mass scale $b = c_0^4/(16\, G\sqrt{\pi G u_0}) \propto \ell_1^2$), integrated with a hand-coded fixed-step RK4 and linear surface interpolation. The two agree to all displayed digits on $M_{\rm crit} = 1.616 \times 10^6\, M_\odot$ at $u_c/u_0 = 14.0$ with $r_s/R = 1.217$, on every tabulated checkpoint (relative difference $< 2\,\%$), and on the distribution statistics of Section 15.2 (median $\log M = 6.10$, $10\,\%$ quantile 5.32, $80\,\%$ half-decade fraction); implementation (ii) confirms the scaling $M_{\rm crit} \propto \ell_1^2$ analytically rather than by a numerical ℓ_1-scan. Both codes and the equilibrium-sequence data are released as supplementary material (see Data Availability); as stated in the Acknowledgments, both originate from the same collaboration and independent third-party verification has not yet been performed.

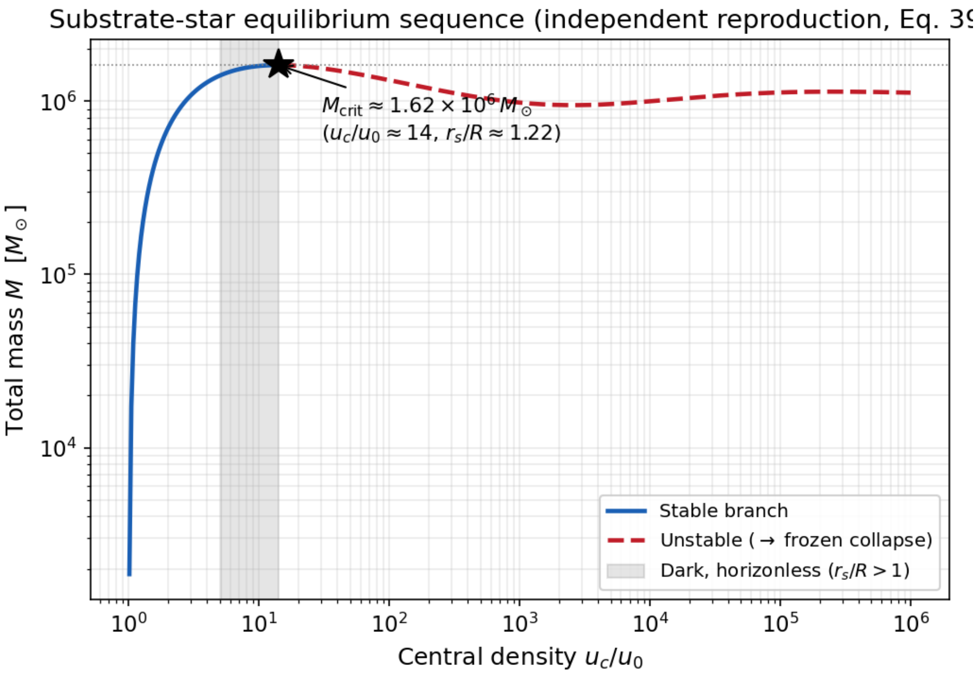

Figure 2: Substrate-star equilibrium sequence $M(u_c)$ from the independent re-integration of the system (39). The stable branch (solid) terminates at the first maximum $M_{\rm crit} \approx 1.62 \times 10^6\, M_\odot$ ($u_c/u_0 \approx 14$, $r_s/R \approx 1.22$); beyond it (dashed), no equilibrium exists and collapse freezes asymptotically. The shaded region marks stable configurations that are dark ($r_s/R > 1$): horizonless objects casting a shadow.

9.2 Numerical Results: Attractor, Critical Mass, and Stability

The numerical integration of the system (39) reveals three structural properties:

1. **Attractor.** Solutions converge toward $M \approx 1.1 \times 10^6\, M_\odot$ at compactness $r_s/R \approx 1.0$, robustly across six orders of magnitude of central density ($r_s \equiv 2GM/c_0^2$).

2. **Photon sphere.** For the exponential metric, the extremum of the impact parameter $b(r) = r\,e^{\chi}$ places the photon sphere exactly at $r_{\rm ph} = 2GM/c_0^2 = r_s$. Any configuration with $R \lesssim r_s$ therefore casts a shadow: a dark object, without horizon.

3. **Stability branch.** The first-maximum criterion of $M(u_c)$ along the sequence of equilibria delimits a continuous stable branch up to a Chandrasekhar-like critical mass:

u_c/u_0	$M\ (M_\odot)$	r_s/R	Status
1.05	2.0×10^4	0.05	stable
1.9	6.2×10^5	0.52	stable
3.3	1.16×10^6	0.84	stable
5.9	1.48×10^6	1.05	stable — dark
14	$\mathbf{1.62 \times 10^6}$	1.22	$M_{\rm crit}$ (limit)
> 14	$< M_{\rm crit}$	~ 1.2	unstable $\to$ freezing

There thus exist *stable* configurations at $r_s/R > 1$: stable dark objects, with a shadow, without horizon or singularity. The compactness increases monotonically along the stable branch and reaches its maximum exactly at the critical point: $(r_s/R)_{\max} = 1.22$ is the maximal compactness of any stable configuration; no stable equilibrium exists beyond it.

Scaling verification and anchor sensitivity. The scaling $M_{\rm crit} \propto \ell_1^2$ is verified numerically to be exact: rerunning the full integration for $\ell_1/\ell_{1,\rm nom} \in \{0.5, 1, 1.63, 4\}$ yields $M_{\rm crit}\,(\ell_{1,\rm nom}/\ell_1)^2 = 1.616 \times 10^6\,M_\odot$ to all displayed digits, with the critical central density $u_c/u_0 \approx 14$ invariant — as required dimensionally, the only mass scale of the system (39) being $c_0^4/\sqrt{G^3 u_0} \propto \ell_1^2$. Since $\ell_1 \propto 1/m_e$, the experimental uncertainty of the anchor propagates as $\delta M_{\rm crit}/M_{\rm crit} = 2\,\delta m_e/m_e \approx 6\times 10^{-10}$ (CODATA), entirely negligible against the modeling uncertainties (Newtonian interior, closure equation of state). Figure 3 displays the verification.

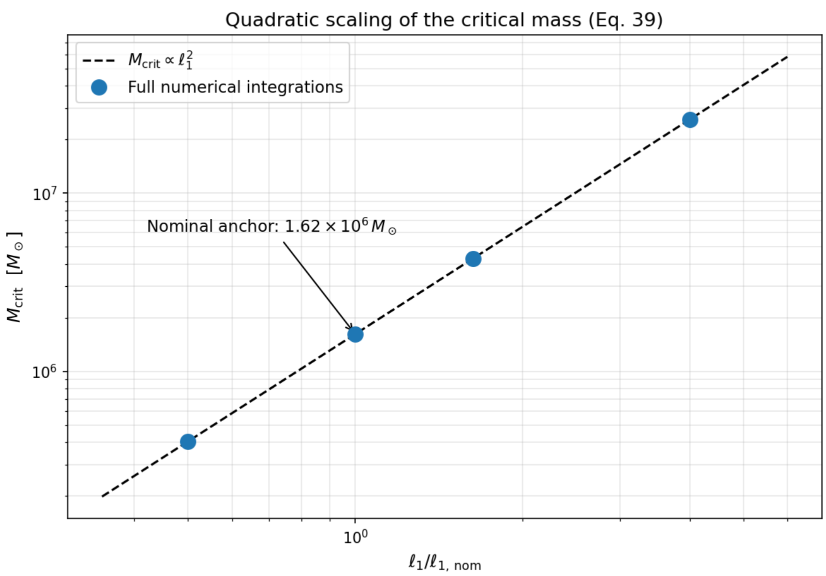

Figure 3: Exact quadratic scaling of the critical mass with the string length: full numerical integrations of the system (39) for $\ell_1/\ell_{1,\rm nom} \in \{0.5, 1, 1.63, 4\}$ (points) against the law $M_{\rm crit} \propto \ell_1^2$ (dashed). The nominal anchor gives $1.62 \times 10^6\,M_\odot$; the point at $\ell_1 \times 1.63$ verifies the scaling law only — the corresponding recalibration is excluded by the thermal-surface argument (Section 9).

Justification of the stability criterion. For a one-parameter sequence of equilibria with a fixed barotropic equation of state, the turning-point theorem identifies the first extremum of $M(u_c)$ with the point of marginal radial stability ($\omega_0^2 = 0$ for the fundamental pulsation mode) [33]: the static first-maximum criterion used here is therefore not merely heuristic but coincides, for this class of sequences, with the dynamical threshold. A direct computation of the radial eigenfrequencies in the DS interior — which requires the covariant reformulation of the matter sector — is retained among the open problems.

The critical mass obeys $M_{\rm crit} \propto \ell_1^2$; the nominal value $\ell_1 = 8.09\times10^{-13}$ m gives $1.6\times10^6\, M_\odot$. The mass scale of galactic dark objects thus emerges from the substrate constants alone (G, c_0, ℓ_1) — a property possessed by no standard exotic compact-object model (gravastar, boson star), whose masses are free parameters [14, 15]. A previously entertained $\times1.63$ recalibration of ℓ_1 (placing Sgr A* at the critical point of the stable branch) is now *excluded* by the thermal-surface argument: a stable substrate star has surface redshift $1 + z = e^{x/2} \leq 1.84$ and no kinematic shield; in steady state it must re-emit its full accretion power (Broderick–Narayan). The non-detection of any thermal surface component from Sgr A* (accretion $\sim 6 \times 10^{38}$ erg/s versus bolometric $\sim 10^{36}$ erg/s) forbids Sgr A* from lying on the stable branch: $M_{\rm crit} < 4.3 \times 10^6\, M_\odot$ strictly. The nominal anchor, with Sgr A* as a Family-3 frozen collapse, is thereby confirmed; frozen collapses themselves escape the thermal-surface test by the same kinematic freeze that silences their echoes (Section 15).

9.3 Frozen Collapses: The Three Families of Dark Objects

Outside the stable branch ($M > M_{\rm crit}$, or stellar objects whose substrate equilibrium would be too diffuse to be dark), there is no equilibrium — but no singularity either. The infall velocity is capped by $c_{eff} = c_0 e^{-\chi}$, which decreases exponentially during compression: the collapse *freezes* asymptotically and no singularity forms in finite time. From the outside, the frozen object is optically indistinguishable from a black hole (practically divergent redshift, shadow, orbits conforming to the exponential metric). The model therefore predicts three families:

- **Family 1** — stellar objects (X-ray binaries, LIGO mergers): frozen collapses;
- **Family 2** — $\sim 10^4$ to $1.6 \times 10^6\, M_\odot$: substrate stars in stable equilibrium (the only family possessing a true surface);
- **Family 3** — supermassive $> M_{\rm crit}$ (Sgr A* marginal, M87*): frozen collapses.

A distinctive prediction of principle: the surface redshift is enormous but finite — a residual radiative leakage exists, exponentially suppressed, qualitatively distinct from GR.

9.4 Debts of the Calculation

The treatment of momentum is Newtonian, marginal at compactness ~ 1 (a covariant reformulation of the matter–substrate sector is required; the conformal representative of the coupling is now fixed, Section 8.2); stability is assessed by the static criterion only; the hypothesis $E = hc_0/\ell$ per cell under compression is a closure postulate; finally, the shear-wave absorption condition at the surface (Section 15) remains undemonstrated.

Part II

Kinematics of Media

10 Mechanics of Non-Local Correlations

10.1 The Phase-Opposition Pair Postulate and Pair Creation

By virtue of the phase-opposition pair postulate, matter creation operates as symmetric pairs rotating in strict phase opposition. These entities share a continuous tension line within the $N_{\mathrm{DS}} = 2$ network, acting as a single resonant LC circuit. Quantum entanglement would be the result of this persistent **topological wiring**.

10.2 The Low-Impedance Corridor and Phase Rigidity

The separation of the particles leaves a compression wake where the dynamic impedance drops sharply but remains *finite*, bounded below by a floor $Z_{\min} = \varepsilon Z_0$ with $\varepsilon \ll 1$. In oscillator-network engineering, the phase readjustment velocity is inversely proportional to this impedance obstacle ($v_\phi \propto 1/Z$), so a low but non-zero $Z_{\min}$ produces a phase synchronization speed

$$v_{\mathrm{sync}} \;=\; c_0 \,\frac{Z_0}{Z_{\min}} \;=\; \frac{c_0}{\varepsilon}, \tag{40}$$

very large but bounded. This finiteness is a structural necessity and a falsifiable handle. Axiom A5 (no pole fusion) guarantees $D > 2r$ at all times, hence $Z_{\mathrm{bif}} > 0$ structurally: the corridor impedance cannot reach zero, and the earlier idealization $Z \to 0$ is replaced throughout by $Z \geq Z_{\min} > 0$. Under this low-impedance condition the loop gain of the distributed PLL becomes very large, though finite, driving the phase evolution toward its Laplacian form

$$\nabla^2 \phi = 0 \tag{41}$$

so that the spatial phase gradient is strongly suppressed and the two extremities of the flux tube synchronize at $v_{\mathrm{sync}} \gg c_0$, forcing the near-instantaneous lock

$$\phi_A(t) \simeq \phi_B(t) \simeq \phi_{\mathrm{wake}}(t). \tag{42}$$

Bell bound on the corridor impedance. The experimental lower bounds on the speed of quantum-correlation enforcement — $v > 1.38 \times 10^4\, c_0$ from the Salart and the Yin *et al.* measurements — translate, via Eq. (40), into an upper bound on the corridor impedance: $\varepsilon \lesssim 10^{-4}$, i.e. $Z_{\min} < 27\ \mathrm{m}\Omega$. The corresponding string separation in the wake follows from the sub-vacuum synchronization relation $v_{\mathrm{sync}}/c_0 = \pi/\operatorname{arccosh}(D/2r)$ and is $\delta = D - 2r <\sim 5 \times 10^{-22}$ m: the two poles approach to within a fraction of the string radius without merging (A5). The predicted v_{sync} — set by the wake-compression versus reactive-wall equilibrium $f_\Gamma \propto |\Gamma_{\mathrm{bif}}|^2$ (Eq. 7) — thereby becomes a new falsification front: any future tightening of the Bell speed bound directly constrains $Z_{\min}$ and δ.

The collapse of the local impedance to its floor short-circuits the spatial delay, permitting the emergence of quantum-mechanical-type correlations and the violation of Bell inequalities without introducing traditional local hidden variables.

The PLL locking of the entangled corridor persists as long as the medium remains purely reactive ($R = 0$). As soon as a measurement occurs, the introduction of a material structure ($N_{\mathrm{DS}} \geq 3$) adds to the impedance a real resistive component R ($Z_{\mathrm{topo}} = R + jX$), acting as a dynamic exchange resistance. This irreversible energy transit injects active power that saturates the local cells, provoking an abrupt PLL unlock (*loss of lock*). This rupture instantaneously destroys the phase alignment, returning the impedance to its rest norm Z_0 and restoring the standard causal delay.

No-signaling. This mechanism structurally forbids any superluminal communication. The common phase $\phi_{\text{wake}}(t)$ is controllable by neither extremity: each local measurement result is dictated by the pre-existing phase state of the corridor and by the local noise of the substrate, hence locally random from the viewpoint of each observer. Any attempt to *modulate* the corridor (to impose information on it) requires coupling a material structure to it, which injects a resistive component and immediately provokes the unlock — the channel is destroyed by the very act that would attempt to use it. Only the *correlations* between results, revealed a posteriori by classical comparison (capped at c_0), carry the trace of the locking: the model thereby reproduces the no-communication theorem of quantum mechanics through an explicit engineering mechanism.

11 Lorentz Invariance as an Emergent Symmetry of the Substrate

The present formalism is of the Lorentz-ether type [7]: length contraction and time dilation follow as exact electrodynamic and hydrodynamic consequences of an oscillating circuit progressing through the DQD gas, in place of the geometric postulate that treats them as intrinsic properties of spacetime.

11.1 The Heaviside Ellipsoid and Convective Impedance

At rest, a matter soliton generates an isotropic spherical impedance profile $Z(r) = Z_0 \exp(2GM/rc_0^2)$. When a soliton ($N_{\text{DS}} \geq 3$) moves at constant velocity v along the x axis, it experiences the dynamic pressure of the substrate. The polarization field of the lattice no longer propagates isotropically, but undergoes longitudinal compression.

The effective radial distance perceived by the lattice dynamics becomes a convective radius r^*, modulated by the elastic Lorentz factor $\gamma = (1 - v^2/c_0^2)^{-1/2}$:

$$r^* = \sqrt{\gamma^2 x^2 + y^2 + z^2} \tag{43}$$

The dynamic impedance of the moving particle flattens into a Heaviside ellipsoid, drastically increasing the reactive energy density on the transverse axis:

$$Z_{mvt}(x, y, z) = Z_0 \exp\left(\frac{2GM}{c_0^2\sqrt{\gamma^2 x^2 + y^2 + z^2}}\right) \tag{44}$$

Verification: this profile is exactly the boosted solution of the static solution of the Lagrangian (26) — the residual of the wave operator $\nabla^2\chi - c_0^{-2}\partial_t^2\chi$ applied to the convective profile is identically null (computer algebra). The Heaviside ellipsoid is therefore not an additional postulate but a consequence of the covariance of the scalar sector (Theorem 3).

To formalize this structural adaptation, we posit a new fluid-dynamics axiom:

A6 — Heaviside Convective Equilibrium. Any soliton ($N_{\text{DS}} \geq 3$) in stationary motion at velocity v mechanically adjusts its internal geometry so that its structural impedance Z_{topo} remains locally matched to the convection flux of the DQD substrate. This pressure produces a physical contraction of the particle by a factor γ along the direction of motion.

11.2 Clock Slowing by Inductive Overload

In this framework a clock (or an atom) is a c_0-confined standing wave: the soliton is a wave folded on itself at the quantization condition $\beta\ell = p\pi$ (Section 6). Its tick is therefore a light-clock, and its slowing under motion follows from geometry alone, with no malleable “time” postulated.

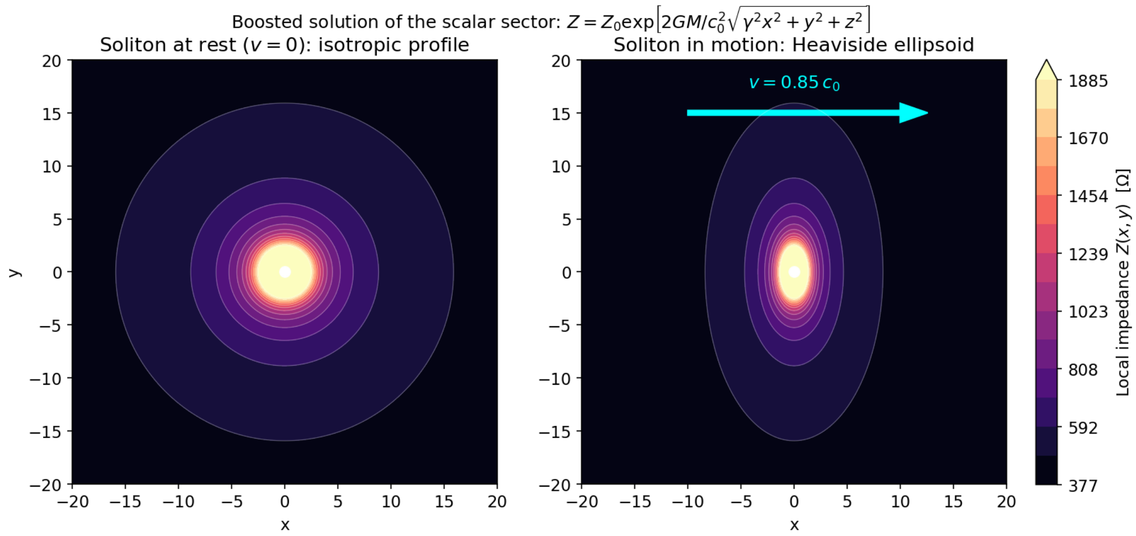

Figure 4: Impedance field of a soliton at rest (left, isotropic exponential profile) and in uniform motion at $v = 0.85\,c_0$ (right): the equal-impedance surfaces contract into the Heaviside ellipsoid, $Z = Z_0 \exp[2GM/c_0^2\sqrt{\gamma^2x^2+y^2+z^2}]$. This profile is the exact boosted solution of the static solution (Theorem 3).

Work in the substrate rest frame, where all internal signals propagate at c_0. A transverse internal cycle (perpendicular to the motion) of a soliton of radius R traverses the Pythagorean path

$$t_\perp = \frac{2R}{c_0}\,\gamma, \tag{45}$$

the standard light-clock result. For the *longitudinal* cycle the outcome depends on whether the soliton contracts. Without contraction, the back-and-forth along the direction of motion gives

$$t_\parallel = \frac{2R}{c_0}\,\gamma^2, \tag{46}$$

so that $t_\parallel \neq t_\perp$: the internal clock would be *anisotropic*, ticking at different rates along and across the motion — an observable directional dependence of atomic frequencies, excluded experimentally. Imposing isotropy $t_\parallel = t_\perp$ forces the longitudinal radius to contract as $R \to R/\gamma$, which is exactly Axiom A6 (Heaviside convective equilibrium). With A6 the longitudinal cycle becomes

$$t_\parallel = \frac{2R}{c_0}\,\gamma, \tag{47}$$

matching Eq. (45). The internal resonance frequency of the moving soliton therefore drops isotropically as

$$\omega' = \frac{\omega_0}{\gamma}, \tag{48}$$

and A6 follows as the condition that the soliton's light-clock remain isotropic — the same argument by which FitzGerald and Lorentz were historically forced to length contraction — rather than standing as an independent postulate. As a corollary, the reactive time constant obeys $\tau \propto \sqrt{L'C'} = \gamma\sqrt{LC}$: the effective $\sqrt{LC}$ dilation emerges as a *consequence* of the light-clock.

Impedance and geometry are one clock. The light-clock and the reactive descriptions of the slowing are the same statement read two ways. The convective compression concentrates the transverse flux lines, raising the cavity inductance by $L \to \gamma^2 L$ while the capacitance stays rigid

($C \propto \rho^0$, Section 8); the reactive period then dilates exactly as $\tau = \sqrt{L'C'} = \gamma\sqrt{LC}$, the cavity impedance rises as $Z_{\text{topo}} \to \gamma\, Z_{\text{topo}}$, and the internal celerity falls as $1/\gamma$ — the confined c_0-wave takes γ times longer to close its loop. This is the moving clock of the light-clock argument, now expressed through the impedance the soliton presents to the substrate. (The Z that carries the clock is the *internal* cavity impedance Z_{topo}, not the external gravitational profile $Z(r)$ of Eq. 26 ff.; time dilation is therefore mass-independent, as required — an electron and a proton at the same v share the same γ.) The earlier reading in which L rose by a single factor γ is superseded: it would give $\tau \propto \gamma^{1/2}$ and hence $\omega' = \omega_0/\sqrt{\gamma}$, whereas the light-clock and the γ^2 inductance compression both yield $\omega' = \omega_0/\gamma$.

In the limit $v \to c_0$ the internal clock stops ($\gamma \to \infty$): only unfolded topologies (no loop, hence no internal clock — $N_{\text{DS}} = 1, 2$) can reach c_0, consistently with the massless-particle table of Appendix B.

The slowing of comoving clocks is thus a pure causal-geometry effect: the internal engine of the particle, being itself a c_0-confined wave, cannot tick faster than its own folded light path allows.

11.3 Demonstration of Emergent Covariance

Consider an interferometer of proper rest length L_0, traveling at velocity v. By virtue of Axiom A6, the standard rod physically contracts according to the exact law $L' = L_0/\gamma$. The absolute round-trip time of light in the instrument writes:

$$t_{tot} = \frac{L'}{c_0 - v} + \frac{L'}{c_0 + v} = \left(\frac{L_0}{\gamma}\right) \frac{2c_0}{c_0^2(1 - v^2/c_0^2)} = \frac{2L_0}{c_0} \cdot \gamma \tag{49}$$

Simultaneously, the local clock of the observer, subject to the inductive overload of the medium, ticks at a rate slowed by a factor γ. The local time t' displayed by the comoving apparatus will therefore be:

$$t' = \frac{t_{tot}}{\gamma} = \frac{2L_0}{c_0} \tag{50}$$

Any local measurement of the speed of light ($c_{measured}$) performed with this contracted rod and this slowed clock will invariably return the nominal celerity of the substrate:

$$c_{measured} = \frac{2L_0}{t'} = c_0 \tag{51}$$

The undetectability of the preferred frame expresses a theorem of perfect elastic equilibrium within the DQD gas, with the laws of classical kinematics left intact.

12 Stability of the Substrate

Purpose. This section records the stability analysis of the substrate. It establishes two constraints having the status of theorems, deduces from them the gaseous nature of the medium, and formalizes the two dynamical axioms (A4, A5) required by the consistency of the whole model.

12.1 Stability Constraints

Theorem 1 (Exclusion of the static lattice). *No static configuration of DQDs maintained by the Coulomb interaction of their poles alone is mechanically stable. An electrostatic potential being harmonic ($\nabla^2 V = 0$), it possesses no local minimum (Earnshaw's theorem).* ***Consequence:*** *the fluctuating character of the substrate is not a descriptive choice but a necessity.*

Theorem 2 (Exclusion of the self-bound liquid). *The substrate cannot condense into a self-bound liquid. The zero-point confinement energy of a massless DQD ($E_{conf} \sim \pi\hbar c_0/\ell$) and the dipolar cohesion energy ($E_{coh} \sim \frac{2}{9}\alpha\,\hbar c_0/\ell$) both decrease as $1/\ell$; their ratio is therefore constant:*

$$\frac{E_{conf}}{E_{coh}} = \frac{9\pi}{2\alpha} \approx 1937. \tag{52}$$

The confinement pressure dominates the cohesion by three orders of magnitude at any density; binding would require $\alpha > 9\pi/2 \approx 14$. ***Consequence:*** *the stability of the vacuum against self-condensation is guaranteed by the smallness of the fine-structure constant.*

Gaseous nature and stability of α. Theorems 1 and 2 impose that the substrate be a gas of free DQDs propagating isotropically at c_0. The density ρ_0, hence $\ell_{\text{cell}} \equiv \nu^{-1/3}$, is there an initial condition and not a quantity fixed by a local equilibrium. A uniform, infinite gas does not dilute (any outflow from a region is statistically compensated): the density remains constant, ensuring the constancy of Z_0, hence of $\alpha = e^2 Z_0/2h$, in agreement with the spectroscopic constraints on the variation of α ($|\Delta\alpha/\alpha| < 10^{-5}$ over the age of the Universe).

Cosmological scope note. The constancy argument of this section (a uniform infinite gas does not dilute) is incompatible with metric expansion, which is independently required by SN Ia light-curve time dilation $\propto (1+z)$, by $T_{\text{CMB}}(z) = T_0(1+z)$, and by primordial nucleosynthesis. Cosmological evolution therefore lies outside the model's scope; where Section 15.2 uses redshifts and distances, it does so on the standard cosmology. A $\rho_0(t)$ history preserving both the constancy of α and the epoch-independence of ℓ_{cell} is an open problem.

12.2 Dynamical Axioms

A4 — Matching principle. The sub-vacuum dynamics relaxes toward impedance matching: the substrate locally minimizes $|\Gamma|^2$. This relaxation law — and not an electrostatic equilibrium — confers on the configuration $\Gamma_{\text{bif}}(D_0) = 0$ the status of a stable attractor, thereby escaping the Earnshaw exclusion (Theorem 1).

A5 — Topological rigidity of the DQD. The DQD possesses no continuous deformation mode. Its only accessible transition is the discrete switch to the micro-loop configuration (neutrino), transient and quantized. The poles of distinct strings do not merge, which forbids the spontaneous condensation of the vacuum into matter. This axiom justifies treating the DQD as a rigid object in the impedance calculations (Section 6) and grounds the origin of ε_0 as an orientational response of the gas, without internal deformation.

12.3 $\mathcal{R}$ as a Derivation Target

In the light of axioms A4 and A5, the three terms of the unified ansatz (Eq. 57) appear as the three regimes of a single law: the fluctuation amplitude of the DQDs adjusts to the local impedance of the traversed medium.

Term of $\mathcal{R}$	Regime	Microscopic brick to derive
$Z_{\text{base}}(1 + 2GM/\lvert x\rvert c_0^2)$	Refractive gravity	Gas compression (Sec. 8, derived)
$\Delta Z(\vec{\Pi}, \varepsilon_{\text{eff}})$	Dielectric response	Orientational statistics $\langle p^2\rangle$ of the gas
$-Z_{\text{base}}\,\beta_{\text{vtx}}^2$	Vorticity	Proper rotation statistics of the cells

Epistemological status. No new numerical value — notably ℓ_{cell} — reaches the *Derived* level at the end of this analysis: the attempted dielectric closures proved dependent on a modeling convention for the deformed impedance, not decided by the current formalism. The acquired result is *structural*: the transformation of $\mathcal{R}$ from a postulated ansatz into a target of microscopic derivation whose missing bricks are explicitly inventoried.

13 Electrodynamic Synthesis: Unified Impedance Ansatz

Epistemological note

The following equation constitutes a first-order phenomenological ansatz. Contrary to the earlier multiplicative approaches, this formalism postulates that each interaction layer (geometric, dielectric, gravitational, and hydrodynamic) articulates as an additive superposition of contributions or electrodynamic potentials defining the state function of space, denoted $\mathcal{R}$:

$$\boxed{R(Z,\Pi,\omega,x) = Z(C,L,x) + \Pi(\vec{\Pi},\epsilon_{\text{eff}},x) + \Omega(\omega,\ell_{\text{cell}},x)} \tag{53}$$

Each component of this sum is defined at every point x of the lattice by:

- **The structural impedance** $Z(C,L,x)$: it describes the base lattice of the vacuum (linked to the inductance L_0 and capacitance C_0), modulated at first order by the refractive-metric solution at position x:
$$Z(C,L,x) = Z_{\text{base}} \exp\left(\frac{2GM}{|x|c_0^2}\right) \tag{54}$$

- **The polarization component** $\Pi(\vec{\Pi},\epsilon_{\text{eff}},x)$: it expresses the local modification of the dynamic dielectric permittivity of the substrate ϵ_{eff} under the effect of the complex polarization vector field $\vec{\Pi}$:
$$\Pi(\vec{\Pi},\epsilon_{\text{eff}},x) = \Delta Z(\vec{\Pi},\epsilon_{\text{eff}}) \tag{55}$$

- **The vorticity component** $\Omega(\omega,\ell_{\text{cell}},x)$: it introduces the kinematic correction linked to the rotation of the DQD cells via the vorticity field ω and the local cell size ℓ_{cell}. This contribution acts purely subtractively via the normalized tangential velocity factor β_{vtx}:
$$\Omega(\omega,\ell_{\text{cell}},x) = -Z_{\text{base}}\left(\frac{\ell_{\text{cell}}^2|\omega|^2}{c_0^2}\right) = -Z_{\text{base}}\beta_{\text{vtx}}^2 \tag{56}$$

In its expanded, first-order-linearized form, the unified additive ansatz writes:

$$R(Z,\Pi,\omega,x) = Z_{\text{base}}\left(1+\frac{2GM}{|x|c_0^2}\right) + \Delta Z(\vec{\Pi},\epsilon_{\text{eff}}) - Z_{\text{base}}\beta_{\text{vtx}}^2 \tag{57}$$

where $\beta_{\text{vtx}} = \ell_{\text{cell}}|\omega|/c_0$ is the normalized vortex velocity factor, strictly bounded in $[0,1[$, expressing the sub-luminal regime of the substrate.

This additive formulation exhibits the vorticity wake as a subtractive term, making explicit why a strong vorticity (ω) induces a drop of the local impedance ($Z < Z_0$), opening the way to the superluminal effect ($c_{\text{eff}} > c_0$) required by the Pump–Probe protocol (whose experimental phenomenology is the subject of Section 15).

13.1 Scale Distinction of the Reflection Coefficients

To avoid any ambiguity on the stability of the lattice reorganized in additive form, we make explicit that the model involves two reflection coefficients operating at distinct physical scales:

- **The sub-vacuum interface coefficient ($\Gamma_{\textbf{pole}}$):** fixed at $\Gamma_{\text{pole}} = 1/3$, it qualifies the local geometric rupture between the unit string ($Z_{\text{half\_dqd}} = Z_0/2$) and the surrounding fluid at rest (Z_0). It is an intrinsic structural property of the interface at the sub-causal scale, guaranteeing the nominal equilibrium spacing of the cell.
- **The dynamic line coefficient ($\Gamma_{\textbf{bif}}(D)$):** it governs the complete DQD cell facing the macroscopic vacuum under an external mechanical constraint. When the spacing D tends toward the core diameter $2r$, the line impedance collapses ($Z_{\text{bif}} \to 0$), driving this coefficient toward total short-circuit mismatch ($|\Gamma_{\text{bif}}| \to 1$) and triggering the stationary restoring force.

13.2 Mechanism of Reactive Confinement Pressure

The restoring force exerted on the walls of the DQD under compression is a reactive confinement pressure, distinct from classical radiation pressure (which is associated with a propagating flux dictated by a Poynting vector). It is interpreted as the direct analogue of the mechanical force exerted on the internal walls of an energized inductor when its geometry is perturbed: the compression of the dielectric micro-cavity neither absorbs nor dissipates active power, and instead compresses the stationary reactive energy density stored sub-vacuum. The surge of counter-pressure is the macroscopic consequence of this purely reactive energy flux opposing the modification of its confinement geometry.

13.3 Intrinsic Limitations of the First-Order Ansatz

As an engineering conjecture, this additive unified ansatz has three major theoretical limits that mark out the model's future developments:

1. **Resolution of the gravitational circularity**: The introduction of the term Z_{base} in the various components implies an implicit dependence on the background impedance Z_0. In the weak field, to avoid any mathematical circularity, this coupling must be treated strictly as a linear relative correction of the refractive metric applied to the base impedance:
$$R(Z, \Pi, \omega, x) \approx Z_{\text{base}} \cdot \left(1 + \frac{2GM}{|x|c_0^2} + \mathcal{O}\left(\frac{GM}{|x|c_0^2}\right)^2\right) + \Delta Z(\vec{\Pi}, \epsilon_{\text{eff}}) - Z_{\text{base}}\beta_{\text{vtx}}^2 \tag{58}$$
2. **Absence of cross-coupling terms**: The purely additive independence of Eq. (53) neglects second-order interactions. In a complete hydrodynamic model, the cell compression induced by the gravitational gradient ($\delta\ell_{\text{cell}}$) locally modifies the fluid velocity profile, which should generate a geometry/vorticity cross term of the type $\delta(\ell_{\text{cell}}) \cdot |\omega|^2$. The omission of this term limits the current ansatz to weak-coupling regimes.
3. **Scalar character of the ansatz:** The state function defined by Eq. (53) is scalar, each component contributing in norm to the effective impedance. Yet the fields $\vec{\Pi}$ and $\vec{\omega}$ define preferred directions in the lattice: a polarized or rotating substrate is intrinsically anisotropic, and its impedance then depends on the polarization of the probe wave. The complete description requires promoting R to an impedance tensor (the polarization term carries the factor Z_{base}, by symmetry with the vorticity term, ensuring homogeneity in ohms):
$$R_{ij}(x) = Z(x)\,\delta_{ij} \;+\; a\,Z_{\text{base}}\,\Pi_i\Pi_j \;-\; b\,Z_{\text{base}}\,\frac{\ell_{\text{cell}}^2\,\omega_i\,\omega_j}{c_0^2} \tag{59}$$
whose trace restores the isotropic scalar ansatz at first order, while the anisotropic terms ($\propto \Pi_i\Pi_j$, $\omega_i\omega_j$) generate two distinct eigen-impedances according to the polarization axis — that is, a birefringence of the vacuum, precisely the observable targeted by the PVLAS and BIREF@HIBEF programs (Section 15). The current scalar formulation is thus limited to isotropic regimes or polarization averages.

13.4 Derivation of the Saturation Coefficient and Atomic Repulsion

Saturation coefficient. The coefficient a of the impedance tensor is no longer free: each DQD cell carries a maximal dipole $p_{\max} = (e/3)\,D_0$ at density $1/\ell_{\text{cell}}^3$, whence the saturation polarization and the coefficient that follows:

$$\Pi_{\text{sat}} = \frac{(e/3)\,D_0}{\ell_{\text{cell}}^3}, \qquad a = \frac{1}{\Pi_{\text{sat}}^2} \qquad \Big(\Pi_{\text{sat}} \approx 2.4 \times 10^4\ \text{C/m}^2 \text{ for } \ell_{\text{cell}} = \ell_1\Big)\,. \tag{60}$$

With the corrected tensor form (factor Z_{base}), full saturation ($|\vec{\Pi}| = \Pi_{\text{sat}}$) produces an order-unity mismatch ($\delta Z \sim Z_{\text{base}}$), the physically expected behavior. This derivation is *conditional* on ℓ_{cell}, the missing brick inventoried in Section 12.

Mechanism and scale of the atomic wall. The reactive wall $\Gamma_{\text{bif}} \to 1$ operates at $\sim 2 \times 10^{-14}$ m: it cannot explain atomic impenetrability at 10^{-10} m. The mechanism at the right scale is **chirality frustration**: when two saturated electronic clouds overlap, the anti-parallel nesting of the tubes becomes impossible (the mechanical analogue of Pauli exclusion), the net $|\vec{\Pi}|^2$ grows with the overlap, Z rises, and the stored reactive energy penalizes interpenetration. This regime is precisely the *non-adiabatic* regime of the criterion of Section 8.4: the Z peak is steep at the very scale of the orbital mode probing it ($L_Z \sim \lambda$), forbidding retuning and forcing reflection. Two numerical bounds fix the scale of the mechanism: drawing the substrate cell energy ($E_1 \approx 1.53$ MeV per cell) would yield $\sim 10^{11}$ eV per atomic overlap (eleven orders of magnitude too strong); Compton-scale field tails would yield a factor e^{-259} at 1 Å (mechanism extinguished). The only coherent closure: the atomic electron being a resonant cavity mode (Section 8) spread at the Bohr scale, its field $\vec{\Pi}$ carries the extension and the exponential decay *of the orbital mode*. Range and magnitude (∼Å, ∼eV) then follow the orbital energetics — structurally isomorphic to Born's exchange repulsion. The substrate supplies the *mechanism*, the orbital supplies the *scale*. The binding case is obtained with no extra ingredient: when the anti-parallel nesting is possible (non-saturated orbitals), $\vec{\Pi}$ locally vanishes, no penalty appears, and the mutual-inductance coupling supplies the attraction — an emergent Lennard-Jones-type potential.

Consistency clause $\chi_{\text{vac}} \ll 1$. If the free vacuum responded with the full saturation polarizability (60), a Petawatt laser ($E \approx 9 \times 10^{14}$ V/m) would produce $\delta Z/Z \sim 5\,\%$, in contradiction with PVLAS and with the estimate $\delta Z/Z \sim 10^{-6}$ of Section 15. The model therefore rigorously distinguishes: the dynamic susceptibility of the free vacuum, $\chi_{\text{vac}} \ll 1$ (ordered phase, rigid PLL, quasi-frozen dipoles — grounded by the nematic order of Section 14), and the field $\vec{\Pi}$ carried by matter, saturated by construction in the tubes.

Epistemological status of the results

This working formalism rigorously distinguishes five levels of theoretical maturity:

- **Derived (Predictive):** the electron characteristic impedance $Z_e \approx 275\ \Omega$; the universal geometric ratio $D/r = 2\cosh(\pi)$; the interface coefficient $\Gamma_{\text{pole}} = 1/3$; the weak-field Schwarzschild refractive index; the exact covariance of the scalar sector and $\alpha_1 = \alpha_2 = 0$ (Theorem 3); the first post-Newtonian parameters $\gamma = \beta = 1$ (Section 8.3); the numerical selection of the force law (30); the identity between this law and the static geodesic of the isotropic conformal representative (Section 8.2); the substrate-star branch with $M_{\text{crit}} \approx 1.6 \times 10^6\, M_\odot \propto \ell_1^2$ and $r_{\text{ph}} = r_s$; the critical impact parameter $b_c = e\, r_s$ (shadow deviation $\delta = +4.63\,\%$); $r_{\text{ISCO}} = \varphi^2 r_s$; the echo delay $\Delta t_{\text{echo}} = (2r_s/c_0)\, e^x/x^2$ with the self-consistency $t_{\text{freeze}} = \Delta t_{\text{echo}}/2$; the Brillouin cutoff $\hbar\omega_{\max} = (3/\pi)\, m_e c^2$; the exact product $E_0 r_0 = e^2/8\pi\varepsilon_0$ with the single-string bound; the semi-classical magneton $\mu = \mu_B$

(a declared half-success: spin ½, $g = 2$, and fermionic statistics are absent); the coefficient $a = 1/\Pi_{\rm sat}^2$ (conditional on $\ell_{\rm cell}$); the uniqueness of the Johns scattering node from the five substrate constraints and the consequent emergence of three-dimensional Maxwell electrodynamics, two transverse polarizations, and the Gauss constraint (Theorem 4, Section 7; conditional on the chiral closure), together with the orthogonality lemma and the geometric chirality of the weave.

- **Calibrated (Adjusted):** the inductance–mass equivalence prefactor κ; the empirical attribution of the fundamental topological indices $N_{\rm DS}$; the anchor $R_3 = \hbar/m_e c_0$ and hence $\ell_1 = 2\pi R_3/3$ (the model's unique experimental anchor, Section 5.2; the formerly entertained recalibration $\times 1.63 \to$ Sgr A* is now excluded, Section 9).
- **Postulated:** A7 (tension chains carrying the TT sector, resting on the nematic order S, with the EM tracelessness clause); A8 (non-gravitating native energy); $E = hc_0/\ell$ under compression; the atomic wall at the orbital-mode scale; the hypothesis $\ell_{\rm cell} \approx \ell_1$ at rest (Section 5); the $\sqrt{r_0/r}$ mutual-inductance law (Eq. 35); the transmission of the weave handedness to the $\pm\frac{1}{2}$ node coefficients (the residual debt of Theorem 4); the distributed phase-lock (PLL) mechanism, invoked without governing equations (Section 16).
- **Reparametrized (Identity):** the internal impedance profiles of the proton ($Z_{\rm proton}$) and neutron ($Z_{\rm neutron}$), which follow directly from the experimental masses reinjected into the consistency relation.
- **Closed / Conceded:** the spin-2 graviton from the scalar/vector fields alone (Z, $\vec{\Pi}$, Ω) — blocked by Helmholtz decomposition and Deser's theorem [27]; the cosmological $w = -1$ sector (the temporal drift of Z gives $w = +1$); photon–electron scattering at all three frequency regimes; any near-horizon reflective surface (LIGO echo bounds, Section 15); surface shear-wave absorption as an echo-survival mechanism (superseded by the kinematic delay); the dynamically adjusting ω_c clause (withdrawn, Section 5).

14 Tensor Sector z_{ij}, Nematic Order, and Spin-2

Preliminary concession. No spin-2 mode can be constructed from the fields Z (scalar), $\vec{\Pi}$ (vector), and Ω (scalar): the Helmholtz decomposition forbids it kinematically, and Deser's theorem [27] closes the dynamical workarounds. This front is explicitly conceded. Yet the observed gravitational radiation is quadrupolar and tensorial (Hulse–Taylor to 0.3 %; the $+/\times$ polarizations of LIGO-Virgo). The complete gravitational sector therefore requires an extension.

14.1 Decomposition and Axiom A7

The impedance is promoted to a tensor, extending the promotion initiated by the tensor R_{ij} of Section 13:

$$Z_{ij} = \bar{Z}\,\delta_{ij} + z_{ij}, \qquad z_{ii} = 0, \quad \partial_i z_{ij} = 0. \tag{61}$$

The trace $\bar{Z}$ is the complete scalar sector, unchanged — a constrained, elliptic mode, the exact parallel of the Newtonian potential in GR. The part z_{ij}, symmetric traceless and transverse, counts two propagating modes: the $+$ and $\times$ polarizations.

A7 — Tension chains and shear rigidity. In its calm, ordered phase the DQD gas organizes into head-to-tail polarization chains under Coulomb tension, characterized by the quadrupolar nematic order parameter S (Section 14 below). These chains confer on the substrate an effective, S-dependent shear modulus; the transverse waves they carry constitute the sector z_{ij}. **Tracelessness clause (exact):** the stress-energy tensor of the chains must be of pure electromagnetic nature, rigorously traceless — no rest-mass component. For an EM flux tube, tension and linear energy density coincide identically, whence $c_T = c_{eff}$ in every frame (the Alfvén mechanism in the massless limit). This clause is not an approximation: a scalar mass loading of fraction δ would produce a velocity deficit $\delta/2$; the GW170817 bound (10^{-15}) excludes even the "natural" loading from Coulomb cohesion treated as mass ($\alpha/18\pi \approx 1.3 \times 10^{-4}$, eleven orders of magnitude above the bound). The integrally EM and massless nature of the substrate makes the cancellation structural, but it now has the status of a survival condition.

The mechanism by which the chains acquire and maintain their coherence is a *candidate*, not a settled part of the axiom: the working hypothesis is a distributed phase-locking (PLL) of the DQD oscillators, but this mechanism is not yet formalized (see the open problem in Section 16). The axiom itself rests only on the nematic order S, a standard orientational order parameter, and does not depend on the microscopic locking mechanism.

14.2 Quadrupolar Nematic Order

A calm region of space permits the statistical alignment of DQD poles; an agitated region disorders them. Two constraints bound the admissible form of this order: Theorem 1 (Earnshaw) forbids any *positional* organization (3D matrix), and a net dipolar alignment would make the vacuum birefringent (excluded by PVLAS and cosmic polarization rotation). The surviving form is a **quadrupolar orientational order** (true nematic): compensated head-to-tail alignment, null net polarization, only the order tensor non-zero:

$$Q_{ij} = S\left(n_i n_j - \tfrac{1}{3}\delta_{ij}\right), \qquad S = S(T), \quad T \propto \langle \Omega^2 \rangle, \tag{62}$$

where S decreases with local agitation. Structural benefits: (i) the shear modulus of A7 becomes S-dependent — the TT rigidity of the calm vacuum *derives from a phase transition* instead of being postulated outright; (ii) the clause $\chi_{\text{vac}} \ll 1$ (Section 13.4) is grounded: ordered phase = high phase rigidity = transparent vacuum; agitated phase near matter = susceptible, relaxation, decoherence.

Condensed-matter precedent. The route "nematic order → massless spin-2 modes" proposed here is not without precedent: Chojnacki et al. [17] have shown, at the level of the action, that the Goldstone modes of quantum spin-nematic phases (realized in magnets and ^{23}Na spinor condensates) are massless spin-2 bosons in one-to-one correspondence with the gravitational waves of linearized gravity, and have outlined an experimental protocol for their observation. This peer-reviewed result establishes that a quadrupolar nematic order parameter generically supports spin-2 wave analogues — precisely the structural claim of Axiom A7 — and substantially de-risks the present construction. The two frameworks differ in substrate and in ambition: Chojnacki et al. work with a lattice of quantum spins (or a spinor condensate) as a laboratory *analogue* of linearized gravity in flat spacetime, whereas the DS model posits an electromagnetic dipole gas as the *actual* carrier of the vacuum's transverse-traceless sector, with the tracelessness clause of A7 enforcing $c_T = c_{eff}$ and the Deser bootstrap driving the sector to full nonlinear GR. The condensed-matter result supplies the kinematic existence proof; the DS-specific content is the identification of the medium, the propagation-speed clause, and the bootstrap endpoint.

Observational content after the bootstrap. A natural question follows (raised in review): if the Deser bootstrap drives the tensor sector to full GR, what does the DS model predict that GR does not? The answer is that the bootstrap fixes the exterior *dynamics*, not the ontology or the limit states. The model's proper observational content survives in four places: (i) the interior sector — the stable substrate-star branch, absent from GR, whose singularity theorems forbid any such equilibrium; (ii) the mass scale $M_{\text{crit}} \propto \ell_1^2$ issued from the substrate constants, with the registered LRD accumulation prediction (Section 15.2); (iii) the surface physics — a finite (if enormous) surface redshift with exponentially suppressed residual radiative leakage, and the shear-absorption condition testable through echo searches; (iv) the strict zero-breathing-mode prediction, plus the 2PN edge-of-testability deviation of Section 8.3, which survives as long as the scalar sector is exactly the exponential metric rather than Schwarzschild.

14.3 Cost of Deser's Theorem and Survival Condition

A field z_{ij} coupled to the stress-energy tensor converges, by the Deser bootstrap, toward the complete Einstein equations: the DS model ceases to be a replacement of GR and becomes a theory of the substrate *beneath* GR (the analogue-gravity posture [9, 10]), in conformity with the epistemological positioning of the Introduction. The quadrupolar coefficient is non-negotiable (Hulse–Taylor, 0.3 %); gravitomagnetism (Lense–Thirring, measured by Gravity Probe B and LAGEOS) must emerge from the bootstrap — not a contradiction but the marker that the bootstrap is obligatory, the endpoint being full GR. The principal danger of the statistical rest frame — the Einstein-aether class, constrained to $\alpha_1 < 10^{-4}$, $\alpha_2 < 10^{-7}$ [30, 29] — is neutralized exactly for the scalar sector (Theorem 3); for the chain sector, the survival condition is the tracelessness clause of A7, which guarantees $c_T = c_{eff}$ in every frame.

Proper predictions of the sector. (i) *Zero breathing mode* in gravitational waves (contrary to scalar-tensor theories): a detection of a *breathing* mode by LIGO-Virgo-KAGRA would falsify this construction. (ii) If cosmological *nematic domains* exist (director $\hat{n}$ coherent over large scales), a birefringence of *gravitational* waves along $\hat{n}$ is expected — weakly constrained to date, domain-averaged isotropy over the paths being required for the model's consistency.

15 Discussion: Experimental Constraints and Falsification Program

Falsification hierarchy. The model's tests, ordered by accessibility and decisiveness: (1) the shadow-diameter deviation $\delta = +4.63\,\%$ (ngEHT; most accessible); (2) the strict zero-breathing-mode prediction (LVK; binary outcome); (3) the hard LRD mass cutoff at M_{crit} with obligatory thermal photosphere (JWST); (4) non-periodic post-merger echoes at exponentially growing spacing; (5) the permanent absence of PBH evaporation bursts (binary outcome); (6) the 2PN pulsar deviation (demoted: masked by the Lense–Thirring term until the moment of inertia is measured).

Photonic Pump–Probe experiment By construction, we know that DQDs allot a relaxation time following a perturbation. It can then be established that the characteristic impedance of the local medium behind a photon will oscillate. The photon first produces a subtle decrease of DQD density. Then, the relaxation of the DQDs recalls a medium at Z_0, except that this stabilization must be elastic and act as a second-order servo system. A characteristic impedance oscillating between Z_0+ and Z_0- means that at a certain point behind the pump photon the speed c will vary between $c - \Delta$ and $c + \Delta$, thereby allowing a speed above c_0.

A low-intensity "Probe" pulse, inserted in the footsteps of the pump with minimal energy so as not to perturb the medium, traverses this zone of modified impedance. Its group velocity c_{eff} then evolves according to the unified relation consistent with refraction:

$$c_{eff} = c_0 \left(\frac{Z_0}{Z} \right) \quad \Rightarrow \quad c_{eff} > c_0 \quad \text{for} \quad Z < Z_0 \tag{63}$$

The principal observable to validate or falsify this model resides in the measurement, by phase or time-of-flight interferometry, of a constant anomalous advance ($\Delta t < 0$) of the probe relative to its out-of-field path. We emphasize that this temporal shift concerns exclusively the **group velocity** within the perturbed wake, preserving the signal front velocity and thereby respecting macroscopic causality in conformity with the Kramers–Kronig relations.

Power scales and technological bounds The amplitude of this wake effect is modeled by a perturbative nonlinear behavior dictated by the squared ratio of field amplitudes $(E/E_S)^2$, where E is the applied electric field and E_S is the Schwinger critical field. Two distinct regimes define the falsifiability of the model:

- **The macroscopic saturation regime:** direct vacuum breakdown and complete rupture of the transmission line require the Schwinger intensity ($\approx 2 \times 10^{29}$ W/cm^2), a threshold technically inaccessible to current engineering.
- **The perturbative interferometric regime:** on existing Petawatt laser installations (of the *Extreme Light Infrastructure* class — ELI), intensities of order 10^{23} W/cm^2 are exploitable. At this power level, the expected relative impedance variation is of order $\delta Z/Z \sim 10^{-6}$ in amplitude. These values lie just below the current constraints on vacuum nonlinearities from birefringence experiments (such as PVLAS or the Euler–Heisenberg predictions), placing the model in a high-precision metrological window, comparable to that of gravitational-wave detectors.

The exact coupling coefficient between the pump-field intensity and the impedance variation δZ not being fixed *a priori* by the static geometry of the model, the fine sensitivity of this effect constitutes an open experimental calibration target.

Position on quantitative vacuum birefringence. The AI-based critical evaluation (SciSpace) requested a quantitative magnetic-birefringence prediction ($\Delta n/B^2$ in T^{-2}) comparable to the PVLAS bound. The honest position of the model is threefold. (i) The DS framework does not at present derive the static Cotton–Mouton coefficient of the vacuum from its cell parameters: the free-vacuum susceptibility χ_{vac} is constrained to be small by the nematic-order clause (Section 13.4) but is not yet computed. (ii) By the model's own epistemological clause (QED exact in its tested domain), the leading-order static birefringence of the DS vacuum is *required* to coincide with the Euler–Heisenberg prediction, $\Delta n \approx 4 \times 10^{-24}\, B^2$ T^{-2} — reproducing this coefficient from the DQD statistics is a stated derivation target, not a free claim; failure to reproduce it, once the microscopic sector is closed, would falsify the model. (iii) The DS-*specific* predictions in this sector lie elsewhere than in a static excess: the resonant substrate response at $E_1 = hc_0/\ell_1 \approx 1.53$ MeV (absent in QED) and a possible excess in light-by-light scattering; any DS deviation from Euler–Heisenberg in static fields is bounded by the current PVLAS sensitivity, $|\Delta n_{\text{DS}} - \Delta n_{\text{EH}}|/B^2 \lesssim 2.5 \times 10^{-23}$ T^{-2} [25]. The model thus makes no static-birefringence claim beyond QED, and is falsifiable in this sector through the MeV resonance channel.

Gravitational constraints and proper predictions The extended gravitational sector of this edition (Sections 9 and 14) comes with its own observational survival conditions:

- **Post-ringdown echoes (LIGO/Virgo):** surface absorption cannot satisfy the echo bounds ($\varepsilon \lesssim 10^{-27}$–$10^{-30}$). An adiabatic taper would require a transition zone $d \gtrsim 10\lambda \approx 134\, r_s$, geometrically untenable; and the kinetic-theory shear viscosity of the saturated interior gives $\omega\eta/\mu = \omega\ell_1/3c_0 \approx 10^{-18}$ at LIGO frequencies, so the surface is a near-perfect mirror ($|\Gamma|^2 = 1 - 5 \times 10^{-9}$). Survival is instead *kinematic*. In the exponential metric, the round-trip echo delay from the photon sphere to a surface of compactness $x = r_s/R$ is

$$\Delta t_{\text{echo}} \simeq \frac{2r_s}{c_0}\,\frac{e^x}{x^2}, \tag{64}$$

exponential in the compactness (versus logarithmic for standard ECOs). The freezing time obeys the same integral, $t_{\text{freeze}}(X) = \Delta t_{\text{echo}}(X)/2$: any object frozen for a time T returns its echo no earlier than $\sim 2T$ (differential pursuit of the receding surface pushes the actual return toward $3T$–$4T$). Astrophysical progenitors, Myr–Gyr old, are therefore structurally silent, with no adjusted parameter. The residual exposure is the fresh merger remnant during its first second ($x \sim 2$–12), whose successive echoes would be spaced at exponentially growing intervals — a non-periodic signature lying outside current quasi-periodic template searches. This limitation of existing searches is independently documented by Vellucci, Franzin and Liberati [19], who show that back-reaction alone already renders ECO echoes non-periodic; the DS signature is distinguished from that mechanism by its functional form — spacing exponential in the compactness, $\Delta t \propto e^x/x^2$, rather than a slow secular drift. The observational exposure of this channel has grown substantially: the expanded LVK catalogue (June 2026) adds 161 binary-black-hole events recorded between April 2024 and January 2025, bringing the total to 390 confirmed detections — each fresh merger remnant being an echo candidate during its first second — and reports the first measurement of three ringdown modes of a single remnant, sharpening the spectroscopic channel adjacent to the zero-breathing-mode prediction. The dedicated remnant tests of the fourth catalog [18] — four of which explicitly search for post-merger echoes — report no evidence for echoes in any analyzed event, consistent with the present framework, in which astrophysically aged progenitors are structurally silent and fresh-remnant echoes fall outside the quasi-periodic templates employed.

- **Shadow diameter (EHT):** the critical impact parameter of the exponential metric is $b_c = e\,r_s = 2.7183\,r_s$, against $(3\sqrt{3}/2)\,r_s = 2.5981\,r_s$ for Schwarzschild: the predicted fractional shadow-diameter deviation is $\delta = +4.63\,\%$. The 2022 EHT measurement of Sgr A* (mass-to-distance priors from GRAVITY/Keck) bounds $\delta = -0.08^{+0.09}_{-0.09}$ (VLTI) and $-0.04^{+0.09}_{-0.10}$ (Keck): the prediction sits within $\sim$1–1.4σ, on the positive side of both central values. Next-generation measurements (345 GHz operations, frequency phase transfer, the Africa Millimetre Telescope, ngEHT; targeted precision $\pm$2–3 %) will decide. *This is the model's most accessible falsification target.*

- **Compact-object mass function (JWST, then LISA):** the stable branch of Section 9 predicts a preferred mass scale near $M_{\text{crit}} \approx 1.6 \times 10^6\,M_\odot$ ($\propto \ell_1^2$). A first confrontation is presented below; on a longer horizon, the LISA sensitivity window for intermediate-mass mergers will test the same scale by the gravitational channel.

- **GW breathing mode:** strict prediction of zero *breathing* mode (Section 14) — a direct falsifier, contrasting with scalar-tensor theories.

15.1 Information and the Absence of Hawking Evaporation

The information paradox requires three ingredients — an event horizon, exactly thermal radiation, and complete evaporation — none of which the model possesses. With $c_{\text{eff}} = c_0 e^{-x}$ never vanishing, no region is causally severed and evolution remains unitary by construction: infalling information is frozen, not destroyed, and becomes accessible on the $\sim 2T$ timescale through the exponentially suppressed residual leakage of Section 9. The cost is that Hawking radiation disappears: an asymptotically frozen collapse emits only a transient Hawking-like flux during formation (Barceló–Liberati–Sonego–Visser class), never a late-time thermal flux nor a final burst. Two falsifiable consequences follow. (i) No primordial-black-hole evaporation burst will ever be observed; a single confirmed detection (HAWC, Fermi) falsifies the model. (ii) Light primordial black holes below 10^{15} g survive to the present day, reopening the evaporation-closed window of the PBH dark-matter parameter space (independent constraints in that mass range remain).

15.2 Confrontation with the Little Red Dot Masses

The revision of the Little Red Dot masses by electron-scattering correction (Rusakov et al. 2026 [31]) brings the population down to $10^{5-7}\,M_\odot$, two orders of magnitude below the earlier virial estimates.

Statistical comparison. The confrontation of the stable branch with this sample gives: theoretical median of the distribution (log-uniform prior in central density) $\log M = 6.10$ (6.096), against $\log M = 6.10$ for the median of the seven firm measurements of the sample. A two-sample Kolmogorov–Smirnov test does not reject the model ($p = 0.11$–0.20 over the prior range); we state explicitly that with $n = 7$ the test has essentially no discriminating power, and we present this as a *consistency check*, not a validation. The pile-up of the 18 fainter objects (median $\log M \lesssim 5.6$) is compatible with the low end of the branch (10 % quantile at $\log M = 5.32$). This result is conditional on the mass-calibration school: under the classical virial estimators ($\log M = 7$–8, the basis of the literature mass function [34]), Family 2 is incompatible by a factor 10–100 as an explanation of the LRDs; the ongoing arbitration in the community will decide this test.

Calibration-robust statement of the prediction. Because the absolute mass scale is under community arbitration, the model's operative prediction is deliberately stated as a property of the *shape* of the mass distribution rather than of its absolute location: a pile-up of objects accumulating toward a maximum followed by a hard cutoff (the caustic of the equilibrium branch, $dM/du_c \to 0$ at the critical point). This shape — accumulation plus cutoff — is detectable within any internally consistent calibration, since it is the Jacobian signature of the branch turnover and not a statement about where in $\log M$ the cutoff falls. A rigid-shift recalibration of the mass scale moves the pile-up bodily without erasing it; only a calibration that is itself non-monotonic in true mass could hide it. The high- versus low-mass arbitration therefore sets *where* the feature sits, not *whether* it exists.

Persistence in redshift. A distinctive structural consequence follows from Family 2 being an *equilibrium* branch: substrate stars have no built-in expiry, and should persist to low redshift, their number declining as the formation channel that populates high central densities becomes rare, while the objects themselves survive. The recent identification of little red dots down to $z \approx 2$, with a gentle decline in number density relative to the $z \sim 5$ peak [35], is qualitatively consistent with this reading of a smoothly declining formation channel. Growth-based scenarios face the converse task of explaining why an accretion mode switches off gradually; the substrate-star reading attributes the decline to a raréfaction of formation, a distinction that a redshift-resolved number-density measurement can eventually probe.

The obligatory photosphere. Conversely, Family-2 substrate stars are accreting objects *without* a kinematic shield: they must display a thermal photosphere. This turns a potential threat into an obligatory signature, consistent with the 2026 “black hole star” phenomenology of the Little Red Dots (dense ionized cocoons, thermal continua, electron-scattering-broadened lines).

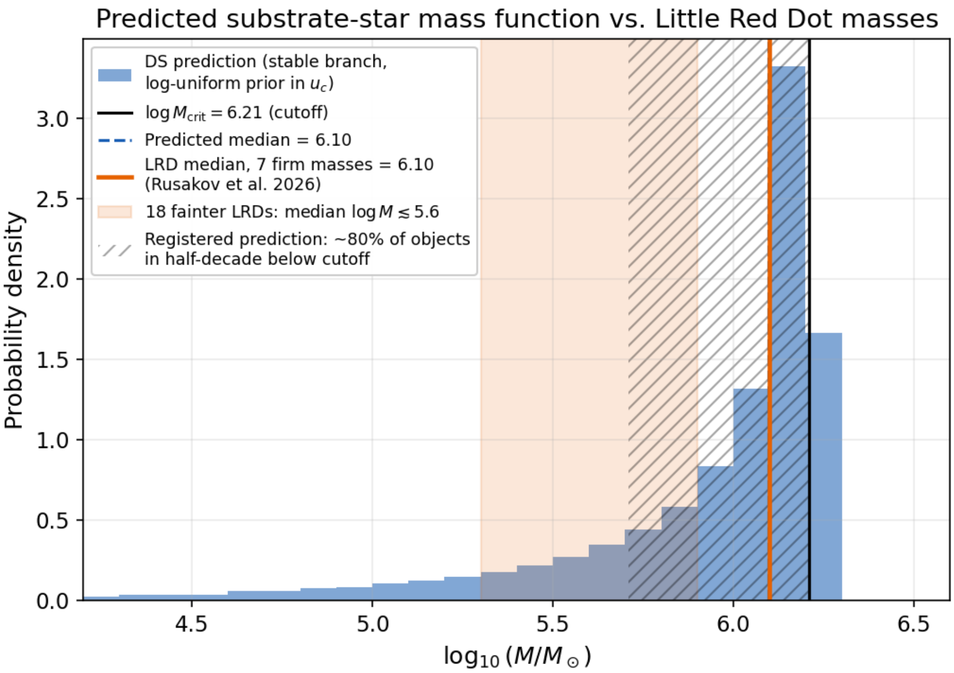

Figure 5: Predicted substrate-star mass function (stable branch of Fig. 2 under a log-uniform prior in central density; blue histogram) confronted with the electron-scattering-corrected Little Red Dot masses of Rusakov et al. [31]. The predicted median ($\log M = 6.10$) coincides with the observed median of the seven firm masses ($\log M = 6.10$; orange line); the band indicates the 18 fainter objects (median $\log M \lesssim 5.6$), compatible with the low end of the branch (10 % quantile at $\log M = 5.32$). The hatched window is the registered prediction: $\sim 80\,\%$ of Family-2 objects in the half-decade below the cutoff at $\log M_{\rm crit} = 6.21$.

Analytic origin and prior-robustness of the accumulation. The accumulation fraction is a caustic effect of the branch geometry, not a numerical accident: since $dM/du_c \to 0$ at the critical point, any smooth prior on the formation parameter u_c piles objects up near $M_{\rm crit}$ under the mapping $u_c \mapsto M(u_c)$. Analytically, for a log-uniform prior on $u_c \in [u_{\rm min}, u_{\rm crit}]$, the fraction in the half-decade below the cutoff is

$$f_{1/2} = \frac{\ln(u_{\rm crit}/u_*)}{\ln(u_{\rm crit}/u_{\rm min})} = \frac{\ln(14.0/1.69)}{\ln(14.0/1.01)} = 0.805, \tag{65}$$

where u_* is the central density at which $M = M_{\rm crit}/\sqrt{10}$. Sensitivity to the prior (verified numerically on the reproduced branch): $f_{1/2} = 80\%$ (log-uniform in u_c), 95% (flat in u_c), 69% (flat in M). The accumulation is thus robust, at the level $f_{1/2} \gtrsim 70\%$, for any smooth prior on the *physical formation parameter*. It is erased ($f_{1/2} = 17\%$) only under a prior imposed flat on the *observable* $\log M$ itself — a choice that cancels the Jacobian by construction and corresponds to no formation channel populating central densities smoothly. The registered figure of $\sim 80\%$ refers to the log-uniform baseline stated at deposit time; the robust, prior-independent statement is the existence of a pile-up with $f_{1/2} \gtrsim 70\%$ followed by a cutoff.

Chandra X-ray constraint. An independent line of evidence bears on the mass-calibration arbitration on which this test is conditional. Sacchi & Bogdán [32] stacked ≈ 400 Ms of Chandra exposure on 55 LRDs and obtained a robust non-detection in the 0.3–7 keV band, ruling out unobscured super-Eddington accretion models unless obscuration is extreme ($N_H \gtrsim 10^{25}$ cm^{-2}, disfavored by JWST spectroscopy); they conclude that the black holes in LRDs are likely *neither as massive nor as luminous* as the virial estimates suggested. This conclusion independently supports the low-mass calibration school (electron-scattering-corrected masses) on which the present confrontation is based, and disfavors the high-mass virial school under which Family 2 would be excluded. The X-ray quietness itself is not in tension with the substrate-star interpretation — the model requires no super-Eddington accretion episode to reach the observed masses, since $M_{\rm crit}$ is a structural scale rather than a growth endpoint; a quantitative accretion-luminosity model for substrate-star surfaces remains future work.

Registered prediction. In the electron-scattering-corrected masses, the model predicts an accumulation of $\sim 80\,\%$ of Family-2 objects in the half-decade below $M_{\rm crit}$ ($5.7 \lesssim \log M \leq 6.21$) followed by a cutoff, whereas direct-collapse heavy-seed scenarios [34] predict no preferred scale — a discriminant accessible to the forthcoming JWST spectroscopic samples. This prediction is time-stamped by the v1.0 Zenodo deposit (version DOI: 10.5281/zenodo.21196099), which predates the relevant future JWST data releases. The statistical criteria of the test are stated above (accumulation fraction, mass window, cutoff); any future modification of these criteria will be documented as a new version under the concept DOI (10.5281/zenodo.21196098), while the frozen record of the present prediction is the v1.0 version DOI above.

Experiments to watch Several ongoing experimental programs offer a direct validation window for the present model, without requiring a dedicated installation. (i) The BIREF@HIBEF collaboration (European XFEL) is preparing a vacuum-birefringence measurement by a pump–probe scheme — Petawatt laser as pump, X-ray beam as probe — structurally analogous to the protocol proposed above; the proof of principle of dark-field detection, validating background suppression at the required level, was published in 2025 [22, 23]. Any excess nonlinear vacuum response beyond the Euler–Heisenberg prediction would constitute a signature compatible with a population of stimulated micro-loops. (ii) The VEGA gamma system at ELI-NP, continuously tunable from 1 to 19.5 MeV with a relative bandwidth below 0.5 %, will eventually permit an energy scan around the predicted cell resonance $E_1 = hc_0/\ell_1 \approx 1.53$ MeV: the DS model predicts a resonant response of the substrate at this energy, where standard quantum electrodynamics predicts no structure. (iii) The ATLAS measurement of light-by-light scattering in ultraperipheral Pb–Pb collisions shows a moderate tension with the theoretical prediction, persistent after full NLO corrections [24] — an excess of the $\gamma\gamma \to \gamma\gamma$ cross section being qualitatively expected for a substrate with excitable micro-loops. (iv) Finally, the PVLAS bounds on vacuum magnetic birefringence [25], and their planned refinement by long-cavity interferometry on the ALPS II magnet string (DESY) [26], constitute the upper calibration constraints that the model's coupling coefficient $\delta Z/Z$ must respect in the static field.

16 Open Problems and Limitations

For transparency toward the reader, the following inventory lists the model's principal open problems, in decreasing order of severity. None of these is glossed over elsewhere in the document; this section gathers them.

1. **Neutrino sector (major).** Three readings all fail against table data: massless unfolded states are excluded by oscillations ($\Delta m^2_{21} = 7.5 \times 10^{-5}$ eV^2, $|\Delta m^2_{31}| = 2.5 \times 10^{-3}$ eV^2); the inductive micro-loop mass $L/\kappa \approx 0.12$–0.58 MeV overshoots $\Sigma m_\nu < 0.12$ eV by $\geq 10^6$; the WKB-weighted effective mass ($p \approx 1.4 \times 10^{-4}$) ≈ 40 eV still overshoots by $\sim$300. One $N_{\mathrm{DS}} = 2$ topology cannot host three flavors ($N_\nu = 2.984 \pm 0.008$, LEP) nor PMNS mixing. A candidate direction — the DQD opening amplitude as the flavor coordinate — is recorded as Postulated, requiring (i) quantization to exactly three levels, (ii) an opening$\to$mass law reproducing the Δm^2 ratio ≈ 33, (iii) a mixing mechanism.

2. **Microscopic derivation of the medium.** The DQD gas and its bifilar transmission-line representation are postulated, not derived from a microscopic Hamiltonian or partition function. Until the distributed RLC parameters are shown to emerge from a well-defined statistical mechanics of DQDs, the model remains, in the apt phrase of the AI-based critical evaluation, a structured set of analogies rather than a physical theory. This is the deepest debt.

3. **Causal structure of the sub-vacuum exchange.** The instantaneous energy exchange within the entangled corridor (Section 10) is explicitly non-local. The no-signaling argument given there is mechanistic, not a theorem: a rigorous demonstration that the operational causal structure of the model coincides with that of special relativity for all observables — beyond the Michelson–Morley argument of Section 11 — remains to be constructed. The model assumes Bell non-locality at the ontological level and claims Lorentz invariance only at the observable level; closing the gap between these two statements formally is required.

4. **Quantitative quantum sector.** The hydrogen spectrum recovery (Section 8) is structural ($E \propto -1/(n^*)^2$), not quantitative: the Rydberg constant is not yet derived from substrate parameters, and no Schrödinger-equation derivation from the phase dynamics has been produced. The claimed emergence of QM is at present interpretive.

5. **Strong-field and radiative gravitational sector.** $\gamma = \beta = 1$ at 1PN (Section 8.3) does not exhaust the comparison with GR. The leading 2PN deviations are now computed ($\Delta g_{00} = -U^3/6$, $\Delta g_{ij} = +U^2\delta_{ij}/2$, Eq. (34)) and placed at the edge of double-pulsar testability ($\sim 10^{-6}$–10^{-5} fractional), but the full 2PN two-body periastron computation remains to be done; the quadrupole formula, GW polarization content beyond the zero-breathing statement, and GW luminosity all await the completion of the tensor-sector bootstrap (Section 14).

6. **Derivation of $\ell_{\mathbf{cell}}$.** The local cell spacing is a cosmological initial condition postulated equal to ℓ_1 at rest; Π_{sat}, ω_c, and the saturation coefficient are conditional on it.

7. **Newtonian interior treatment.** The hydrostatic integration of Section 9 treats momentum non-relativistically at compactness ~ 1; a covariant reformulation could shift M_{crit}.

8. **Statistical power of the LRD test.** The present sample ($n = 7$ firm masses) cannot discriminate; the registered prediction (Section 15.2) is the operative test.

9. **Formalization of the distributed phase-lock.** The phase-locking (PLL) mechanism invoked to confer coherence on the substrate — lattice rigidity (Section 3), the entangled corridor (Section 10), the transparency clause $\chi_{\text{vac}} \ll 1$ (Section 13.4), and the nematic order underlying A7 (Section 14) — is at present a name imported from electronics, without governing equations. The natural formalization is a distributed injection-locking / Kuramoto dynamics on the DQD gas, with the coupling supplied by the pole reflections Γ_{pole} and the whole read as axiom A4 (relaxation toward $|\Gamma|^2$ minimum) in servomechanism form; deriving the phase stiffness ρ_ϕ from this dynamics — and with it $\langle \delta Z^2 \rangle$, χ_{vac}, and the shear modulus in one stroke — is a stated target.

10. **Chiral closure of the Maxwell-3D node.** The uniqueness theorem for the 3-DQD node (Section 7, Theorem 4) is conditional on a single residual postulate: that the geometric handedness of the three-line weave transmits to the $\pm\frac{1}{2}$ scattering coefficients. This requires a dynamical diffusion calculation on the interlocked crossing and is not completed here.

11. **Derivation of G — reclassified from target to demonstrated obstruction.** The equation of state $P = u/3$ makes the substrate conformally invariant: it possesses no intrinsic scale and can generate no dimensionless number of order $3/4\alpha \approx 103$. Three mechanisms (residual dephasing via A5, transition frequency, neutrino-conformation duty cycle) all cap at action $S = O(h)$ because $E_1 \ell_1 = hc_0$. Unlocking G would require an independently derived conformal-breaking scale, absent from the model. The empirical identity $G = 1.084\,(hc_0/9m_e^2)\,e^{-3/4\alpha}$ (accurate to 10^{-4}, non-circular) is retained as an unexplained fact.

12. **Charge as chirality: pair creation and the P–C identification.** With charge carried by winding chirality, three structural consequences follow. (i) The vacuum node being achiral (Theorem 4, O_h-invariant scattering), net chirality is conserved and equal to zero; chiral solitons can therefore only be created in mirror pairs. Charge conservation, already verified at the node level (constraint C2), thereby acquires a second, topological root. (ii) Annihilation becomes mechanical: two mirror windings meeting untwist into the achiral vacuum, releasing their energy as achiral $N_{\text{DS}} = 1$ solitons. (iii) Spatial inversion exchanges the two winding senses (Section 7.5: $-\nVdash$ maps the two weaves onto each other); parity therefore *acts as* charge conjugation — the mirror image of an electron is a positron. This identification is invisible to the emergent electromagnetic sector, which respects P and C separately; any contact with the weak sector, where P and C are separately violated, lies outside the model's scope. The declared debt of this construction is cosmological: strict pair creation implies exact matter–antimatter symmetry at formation, making the observed baryon asymmetry an open problem of the framework, as it is of the Standard Model.

13. **Genesis conjecture (unconstrained).** The primitive state is conjectured to be the defect-free cubic lattice of Section 5.1; a quench during its condensation (Kibble–Zurek mechanism) would freeze in chiral loop defects by pairwise string reconnection — a mechanism that produces closed, chiral loops with a minimum circumference $\sim \ell_1$, consistent with a discrete stable spectrum. Neither the quench nor the reconnection dynamics is

derived; the entry records a research direction, not a result. The behaviour of a fixed-ℓ_1 lattice under cosmological expansion is a second open question of the same sector.

14. **Proton characteristic impedance — open derivation.** The mass law $m \propto N_{\rm DS}^2 Z_{N_{\rm DS}}$ with $m_p/m_e = 1836$ and $N_p/N_e = 9$ requires $Z_p/Z_e \approx 22.7$ (the same factor already appearing as the current ratio $I_p = 22.7\, I_e$ in Section 8). A closed toroidal-helix geometry for the $N_{\rm DS} = 27$ soliton (9 turns of 3 strings, mutual inductance $L \propto N^2$, series inter-turn capacitance $C \propto 1/N$) yields $Z_p/Z_e = N^{3/2} = 27$ — within 19 % of the required value, a residual of logarithmic order comparable to the $\ln(8R_3/r)$ corrections of the electron derivation. Closing this gap from an internal matching condition, without fitting, would render the proton mass geometric; the derivation is open.

15. **Rotation sector.** The model is static; real compact objects spin, and Blandford–Znajek jet launching requires an ergosphere. The vorticity field of the ansatz ($-Z_{\rm base}\beta_{\rm vtx}^2$, lowering local impedance) is the natural frame-dragging analogue; a "Kerr analogue" (frozen collapse + frozen vorticity) is an open construction. Jets themselves pose no conflict (launched outside the photon sphere).

16. **Semiclassical formation flux.** The transient Hawking-like emission during collapse (BLSV class) requires curved-space QFT beyond the present framework.

17 General Conclusion

The Dipolar Strings physics presented in this document is an exploratory, phenomenological model that approaches the nature of matter and vacuum through an analogical mechanics anchored in transmission-line electrodynamics. By imagining space as a capacitive and inductive (LC) physical substrate where point particles give way to simple topological nodes, new perspectives take shape.

This edition proposes the common physical level beneath General Relativity and Quantum Mechanics — both held exact in their domains — a single ontology underlying the two pillars at once. Beneath GR, the DS model *extends*: where the singularity theorems mark the end of validity of the Einsteinian continuum, the substrate takes over and delivers finite equilibria — a stable branch of substrate stars without horizon or singularity, endowed with a preferred mass scale $M_{\rm crit} \propto \ell_1^2$ issued from the medium's constants alone, and frozen collapses everywhere else. Beneath QM, the DS model *interprets*: orbital quantization, exclusion, measurement, and entanglement receive a deterministic, explicitly non-local impedance mechanics. The asymmetry of maturity between these two arms is assumed: quantitative on the gravity side, interpretive on the quantum side.

Broader impact. Beyond its specific claims, this program bears on three wider questions. For astrophysics, a confirmed preferred mass scale in the compact-object mass function would reshape the seeding problem of supermassive black holes, replacing growth histories with a structural attractor. For foundations, the model is a concrete test case of how far the analogue-gravity paradigm [9, 10] can be pushed from laboratory analogy toward candidate ontology, and of what evidential standards such attempts must meet — the fully AI-mediated revision trajectory of this document, preserved in Appendix A, is offered as a methodological data point in itself. For scientific practice, the manuscript documents a fully disclosed human-AI collaboration protocol (falsification-partner mode, independent re-implementation, symbolic verification) that may be useful to other independent researchers; its limitations — chiefly, that both numerical implementations originate from the same collaboration — are stated rather than hidden. The speculative status of the model is reaffirmed: nothing in this document should be read as a validated contribution until the designated falsification targets have been confronted with data.

The path from coherent analogue model to validated physics passes through a quantitative prediction before the measurement: the shadow-diameter deviation $\delta = +4.63\,\%$ (ngEHT) is the most accessible target, and the mass function of intermediate-mass compact objects near $M_{\rm crit}$ (JWST, then the LISA window) the structural one. Until then, this working model constitutes an alternative modeling whose relation to General Relativity is intended to parallel the relation of molecular theory to continuum hydrodynamics: not a contradiction, but a candidate microstructure for a continuum theory that is exact in its domain.

Data Availability

This manuscript, together with its supplementary files, is archived on Zenodo under the concept DOI 10.5281/zenodo.21196098 (which always resolves to the latest version); the v1.0 version DOI 10.5281/zenodo.21196099 serves as the time-stamped record of the registered prediction of Section 15.2. The supplementary files of the present version include: the two independent implementations of the hydrostatic equilibrium integration (Section 9) and the equilibrium-sequence data; the figure-generation scripts (Figs. 2, 5, 4); and the SymPy scripts for the symbolic verifications (the 1PN/2PN expansions of Section 8.3; Theorem 3, the conformal identity $g_{\rm iso} = e^{\chi} g$, and the boosted-solution residual). All numerical results are reproducible from the structure equations (39), which fully specify the integration.

Acknowledgments and Methodological Disclosure

The development of this work was carried out in extensive collaboration with Claude (Anthropic), used as a computational assistant, critical falsification partner ("guard-rail"), and writing assistant, under the direction of the author. The founding physical intuition (the vacuum as an impedance-matched transmission-line network), the dipolar-string concept, and the transmission-line derivations of Sections 5.1–5.2 originate with the author, an electrical engineer. The general-relativistic and field-theoretic formalization — including Theorem 3, the conformal-representative analysis, the post-Newtonian expansions, the tensor-sector construction, the hydrostatic integrations and their re-implementation, the statistical analyses, and the English text — was generated primarily by the AI assistant in response to successive rounds of AI-based critical evaluation (SciSpace), and the author does not claim independent command of this layer. All research decisions and the decision to archive this document are the author's. The document is offered as an exploratory working hypothesis and a documented case study of AI-assisted independent research — not as a validated contribution or a claim of expertise in general relativity or quantum field theory on the author's part. Both numerical implementations originate from this same collaboration; independent third-party verification has not yet been performed, and the reader is invited to reproduce the results from the structure equations (39) and the released code.

All external critical evaluation of this manuscript was performed by an AI-based review tool (SciSpace, formerly Typeset), operating independently of the primary AI collaborator (Claude, Anthropic). **No human peer review has taken place at this stage.** The revision trajectory preserved in Appendix A therefore documents an entirely AI-mediated revision process, disclosed here as part of the manuscript's fully declared human–AI collaboration protocol.

A Document History

This article consolidates a sequence of working documents (V1.8 through V2.5, 2025–2026) developed through several rounds of AI-based critical evaluation (SciSpace; no human peer review has taken place). The complete version-by-version change log — including all errata, closed research fronts (spin-2 from scalar/vector fields, the $w = -1$ cosmological sector, photon–electron scattering, near-horizon reflective surfaces), and the AI-mediated revision trajectory — is archived with the versioned Zenodo record of this manuscript (concept DOI: 10.5281/zenodo.21196098). The registered prediction of Section 15.2 is time-stamped by the Zenodo deposit accompanying this article; its statistical criteria are frozen as stated in that record.

B Fundamental Table of Elementary Particles

The table below is a reverse-engineered parametrization, not a set of predictions; see the Scope statement of Section 1. In line with that statement — the framework is a theory of the medium, not of matter — this edition retains only the three states within scope: the photon ($N_{\mathrm{DS}} = 1$ soliton), the DQD constituent of the vacuum ($N_{\mathrm{DS}} = 2$), and the electron ($N_{\mathrm{DS}} = 3$), the model's unique calibration anchor. The previously tabulated assignments for the muon, tau, and the weak bosons (W, Z, H) were reverse-engineered mass fits without predictive content and are withdrawn from the catalogue.

Remark (Warning — calibrated catalogue, not predictions)*.* The index assignments in this table are the result of phenomenological reverse engineering against the experimental masses, under the charge-quantization constraint. They are working hypotheses of the exploratory framework A1 — *none* of the entries below constitutes a prediction of the model, and the table must not be read as one. The model's predictive content resides in the derived quantities listed in the epistemological status classification (Section 13), not here.

Methodological note on the calibration of the indices For development purposes, we have elaborated a postulated N_{DS} index system, fully assumed as a working framework. In this formalization, it is posited that charge is dictated topologically by the *winding chirality* of the closed loop — the two mirror senses of circulation carrying opposite signs, with the magnitude $e/3$ per string fixed independently by the interface coefficient $\Gamma_{\mathrm{pole}} = 1/3$ (Section 5.1) — and that mass follows from a closed-loop weight. All solitons of the catalogue are closed structures; no open terminations are invoked. This assignment answers the question left open in Section 7.5: the geometric chirality of the weave, mute at the level of the electromagnetic scattering, is physically relevant at the soliton level, where it carries the sign of the charge. The catalogue is consistent under this rule: the two neutral states in scope ($N_{\mathrm{DS}} = 1, 2$) are achiral, the charged state ($N_{\mathrm{DS}} = 3$) is chiral. The indices and associated configurations were isolated by phenomenological reverse engineering, articulating the strict constraint of the charge-quantization formula $Q_{eff} \sim \frac{N_{\mathrm{DS}} \pmod 4}{3} e$ with the scale of the experimental masses. This restricted catalogue is a working framework, not a predictive base; a direct analytic derivation of lepton mass ratios from the mechanical equilibrium equations of the strings, without recourse to the free prefactor κ, remains the stated (and unmet) target that would be required before any heavier state could be readmitted.

State (N_{DS}, p)	**Particle**	**Symbol**	**Mass**	**Charge**	N_{DS} mod 4	**Geometric configuration**
(1,1)	Photon	γ	0	0	1	Unfolded unit string, massless linear transmitter.

State (N_{DS}, p)	**Particle**	**Symbol**	**Mass**	**Charge**	N_{DS} mod 4	**Geometric configuration**
(2,1)	Dipolar Quantum Double	–	0	0	2	Head-to-tail doublet at rest, perfect matching $Z_{\mathrm{bif}} = Z_0$.
(3,1)	Electron	$e^{\pm}$	0.511 MeV	± 1	3	First closed soliton, loose circular winding ($R_3/r \approx 37.1$) at the fundamental radial mode.

C Nomenclature and Units of Variables

Symbol	Description	Unit (SI/practical)
Constants and Fundamental Substrate		
c_0	Intrinsic speed of light (DQD exchange kinematics)	m/s
Z_0	Fundamental characteristic impedance of the vacuum ($\approx 377\ \Omega$)	Ω (Ohm)
L_0	Fundamental inductance of the vacuum	H (Henry)
C_0	Fundamental capacitance of the spatial dielectric	F (Farad)
ϵ_0	Electric permittivity of the vacuum	F/m
μ_0	Magnetic permeability of the vacuum	H/m
e	Elementary electric charge	C (Coulomb)
α	Fine-structure constant ($\approx 1/137.036$)	Dimensionless
$\hbar$	Reduced Planck constant	J·s
k_B	Boltzmann constant	J/K
Geometry of the DQD Substrate		
r	Tube radius of the elementary string ($\approx 1.04 \times 10^{-14}$ m)	m
D	Rest-invariant spacing between strings from matching ($D/r = 2\cosh(\pi) \approx 23.18$)	m
ℓ_1	Nominal length of a fundamental string ($\ell_1 = 2\pi R_3/3 \approx 8.09 \times 10^{-13}$ m; model constant)	m
ℓ_{eff}	Effective near-field interaction length (reconciled)	m
$R_{N_{\text{DS}}}$	Topological major radius of a particle of index N_{DS}	m
R_3	Major radius of the reference electron ($= \hbar/m_e c_0 \approx 3.861 \times 10^{-13}$ m; unique calibrated anchor, Sec. 5.2)	m
λ_C	Compton wavelength ($= 2\pi R_3$ for the electron)	m
R_{mass}	Gravitational topological footprint radius ($= GM/c_0^2$)	m
Local Dynamical Fields		
$Z(\vec{x}, t)$	Local complex dynamic impedance of the substrate	Ω
$\vec{\Pi}(\vec{x}, t)$	Complex polarization vector field	C/m^2
$\Omega(\vec{x}, t)$	Scalar vorticity-density field	s^{-1}
$\phi(\vec{x}, t)$	Intrinsic phase of the polarization field	rad
$\nu(\vec{x})$	Local DQD number density	m^{-3}
$\ell_{\text{cell}}(\vec{x})$	Local, fluctuating inter-cell spacing of the substrate ($\equiv \nu^{-1/3}$; $\approx \ell_1$ at rest, working hypothesis)	m
$c_{eff}(\vec{x}, t)$	Local effective propagation celerity	m/s
n	Dynamic refractive index of the vacuum ($= Z/Z_0 = c_0/c_{eff}$)	Dimensionless
β_{vtx}	Normalized sub-luminal vortex velocity factor	Dimensionless
Particle Impedances and Mismatch		
$Z_{N_{\text{DS}}}$	Topological impedance of a particle of index N_{DS}	Ω
$Z_{\text{half\_dqd}}$	Local impedance of a unit string facing the neutral plane ($\approx 188.5\ \Omega$ at rest)	Ω
Z_{in}	Reactive input impedance of the closed-loop structure	Ω

Symbol	Description	Unit (SI/practical)
$L_{N_{\rm DS}}$	Topological confinement inductance ($= \kappa\, M_{DS}$)	H
$C_{N_{\rm DS}}$	Geometric capacitance of the topological torus	F
κ	Inductance–mass equivalence constant (calibrated free parameter)	H/MeV
Γ	Internal impedance reflection coefficient	Dimensionless
Topological Properties of Matter		
$N_{\rm DS}$	Topological index (number of dipolar strings of the structure; strings indexed by $i = 1 \dots N_{\rm DS}$)	Dimensionless
p	Second quantum number designating the radial constriction mode	Dimensionless
n^*	Stationary harmonic mode index (orbital energy level)	Dimensionless
M_{DS}	Total topological mass (inductive equivalence)	MeV/c^2
Q_{eff}	Invariant apparent charge (winding-chirality asymmetry)	C
$\tilde{\omega}$	Topological rotation angular velocity of the node	rad/s
Decays and Topology		
k	Stoichiometric equilibrium factor of decays	Dimensionless
N_{DQD}	Number of DQD pairs absorbed or emitted in a decay (a count of DQD *pairs*; to be distinguished from the string index $N_{\rm DS}$)	Dimensionless
Strong-Field and Tensor Gravitational Sector		
χ	Logarithmic impedance potential ($\equiv \ln(Z/Z_0)$; $= 2GM/rc_0^2$ in the exterior)	Dimensionless
Φ	Gravitational potential ($\equiv -\frac{c_0^2}{2}\ln(Z/Z_0)$; $= -GM/r$ in the exterior)	m^2/s^2
U	Dimensionless Newtonian potential ($\equiv GM/rc_0^2$; PPN expansion parameter, Sec. 8.3)	Dimensionless
$\gamma,\ \beta$	First post-Newtonian parameters ($= 1$ in this model, Sec. 8.3)	Dimensionless
L_Z	Characteristic length of the impedance gradient ($\equiv \lvert\nabla \ln Z\rvert^{-1}$, adiabaticity criterion, Sec. 8.4)	m
u_0	Native rest energy density of the vacuum ($= hc_0/\ell_1^4 \approx 4.6 \times 10^{23}$ J/m^3)	J/m^3
$M_{\rm crit}$	Critical mass of the stable substrate-star branch ($\approx 1.6 \times 10^6\, M_\odot$, $\propto \ell_1^2$)	kg
r_s	Nominal Schwarzschild radius ($= 2GM/c_0^2$)	m
$r_{\rm ph}$	Photon-sphere radius of the exponential metric ($= r_s$)	m
z_{ij}	Transverse traceless tensor part of the impedance ($Z_{ij} = \bar{Z}\delta_{ij} + z_{ij}$)	Ω
$\Pi_{\rm sat}$	Saturation polarization of the dipolar gas ($= (e/3)D_0/\ell_{\rm cell}^3$)	C/m^2
S, Q_{ij}	Quadrupolar nematic order parameter and tensor ($Q_{ij} = S(n_i n_j - \delta_{ij}/3)$)	Dimensionless
c_T	Shear-wave speed of the tension chains ($= c_{eff}$ by EM tracelessness)	m/s

References

[1] S. Navas *et al.* (Particle Data Group), *Review of Particle Physics*, Phys. Rev. D **110**, 030001 (2024).

[2] D. J. Griffiths, *Introduction to Electrodynamics*, 4th ed., Cambridge University Press, 2017.

[3] D. M. Pozar, *Microwave Engineering*, 4th ed., John Wiley & Sons, 2011.

[4] A. Taflove and S. C. Hagness, *Computational Electrodynamics: The Finite-Difference Time-Domain Method*, 3rd ed., Artech House, 2005.

[5] P. B. Johns and R. L. Beurle, *Numerical solution of 2-dimensional scattering problems using a transmission-line matrix*, Proc. IEE **118**(9), 1203–1208 (1971).

[6] P. B. Johns, *A symmetrical condensed node for the TLM method*, IEEE Trans. Microwave Theory Tech. **35**(4), 370–377 (1987).

[7] A. Einstein, *Äther und Relativitätstheorie*, Julius Springer, Berlin, 1920.

[8] H. E. Puthoff, *Polarizable-Vacuum (PV) Approach to General Relativity*, Found. Phys. **32**, 927–943 (2002).

[9] C. Barceló, S. Liberati, and M. Visser, *Analogue Gravity*, Living Rev. Relativity **14**, 3 (2011).

[10] G. E. Volovik, *The Universe in a Helium Droplet*, Oxford University Press, 2003.

[11] A. D. Sakharov, *Vacuum quantum fluctuations in curved space and the theory of gravitation*, Sov. Phys. Dokl. **12**, 1040 (1968).

[12] T. Jacobson, *Thermodynamics of Spacetime: The Einstein Equation of State*, Phys. Rev. Lett. **75**, 1260 (1995).

[13] E. Verlinde, *On the Origin of Gravity and the Laws of Newton*, JHEP **2011**, 29 (2011).

[14] P. O. Mazur and E. Mottola, *Gravitational Condensate Stars: An Alternative to Black Holes*, arXiv:gr-qc/0109035 (2001).

[15] P. O. Mazur and E. Mottola, *Gravitational Condensate Stars: An Alternative to Black Holes*, Universe **9**, 88 (2023).

[16] H. Katayama, N. Hatakenaka, and K.-i. Matsuda, *Analogue Hawking Radiation in Nonlinear LC Transmission Lines*, Universe **7**, 334 (2021).

[17] L. Chojnacki, R. Pohle, H. Yan, Y. Akagi, and N. Shannon, *Gravitational wave analogs in spin nematics and cold atoms*, Phys. Rev. B **109**, L220407 (2024); arXiv:2310.10078.

[18] A. G. Abac *et al.* (LIGO Scientific, Virgo, KAGRA Collaborations), *GWTC-4.0: Tests of General Relativity. III. Tests of the Remnants* (2026). arXiv:2603.19021.

[19] V. Vellucci, E. Franzin, S. Liberati, *Echoes from backreacting exotic compact objects*, arXiv:2205.14170 [gr-qc] (2023).

[20] F. Bosa, *Theory of Spacetime Impedance: A Reactive Framework for the Electromagnetic, Gravitational, and Quantum Structure of the Vacuum*, Quantum Rep. **8**(1), 25 (2026). DOI: 10.3390/quantum8010025.

[21] H. G. Flores, *RLC Electrical Modelling of Black Hole and Early Universe: Generalization of Boltzmann's Constant in Curved Space-Time*, Preprints.org 202305.2246 (2023). DOI: 10.20944/preprints202305.2246.

[22] N. Ahmadiniaz *et al.*, *Towards a vacuum birefringence experiment at the Helmholtz International Beamline for Extreme Fields* (Letter of Intent, BIREF@HIBEF), High Power Laser Sci. Eng. **13**, e7 (2025).

[23] M. Šmíd *et al.*, *Proof-of-principle experiment for the dark-field detection concept for measuring vacuum birefringence*, Phys. Rev. A **112**, 063512 (2025); arXiv:2506.11649.

[24] Ajjath A. H., E. Chaubey, M. Fraaije, V. Hirschi, and H.-S. Shao, *Light-by-Light Scattering at Next-to-Leading Order in QCD and QED*, Phys. Lett. B **851**, 138555 (2024); arXiv:2312.16956.

[25] A. Ejlli *et al.*, *The PVLAS experiment: a 25 year effort to measure vacuum magnetic birefringence*, Phys. Rep. **871**, 1–74 (2020).

[26] A. D. Spector, T. Kozlowski, and L. Roberts, *Demonstration of an interferometric technique for measuring vacuum magnetic birefringence with an optical cavity*, Phys. Rev. A **113**, 063518 (2026); arXiv:2510.14064.

[27] S. Deser, *Self-interaction and gauge invariance*, Gen. Relativ. Gravit. **1**, 9–18 (1970).

[28] B. P. Abbott *et al.* (LIGO Scientific Collaboration, Virgo Collaboration, Fermi-GBM, INTEGRAL), *Gravitational Waves and Gamma-Rays from a Binary Neutron Star Merger: GW170817 and GRB 170817A*, Astrophys. J. Lett. **848**, L13 (2017).

[29] C. M. Will, *The Confrontation between General Relativity and Experiment*, Living Rev. Relativity **17**, 4 (2014).

[30] T. Jacobson, *Einstein-aether gravity: a status report*, PoS QG-PH:020, arXiv:0801.1547 (2008).

[31] V. Rusakov, D. Watson, G. P. Nikopoulos, *et al.*, *Little red dots as young supermassive black holes in dense ionized cocoons*, Nature **649**(8097), 574–579 (2026). DOI: 10.1038/s41586-025-09900-4; arXiv:2503.16595.

[32] A. Sacchi and Á. Bogdán, *Chandra Rules Out Super-Eddington Accretion Models for Little Red Dots*, Astrophys. J. Lett. (2025). DOI: 10.3847/2041-8213/adf5c8; arXiv:2505.09669.

[33] S. L. Shapiro and S. A. Teukolsky, *Black Holes, White Dwarfs, and Neutron Stars: The Physics of Compact Objects*, Wiley, 1983.

[34] J. Jeon, B. Liu, V. Bromm, *et al.*, *Little Red Dots and their Progenitors from Direct Collapse Black Holes*, Astrophys. J. **998**, 148 (2026). DOI: 10.3847/1538-4357/ae3725; arXiv:2508.14155.

[35] S. Kapoor, J. Matthee, A. Torralba, *et al.*, *Little Red Dots at $z \sim 2$ in EIGER reveal a gentle decline with respect to their peak number density at $z \sim 5$*, arXiv:2607.00084 (2026).